Three-dimensional theory of emittance in Compton scattering and x-ray protein crystallography

F. V. Hartemann,[1] H. A. Baldis,[1,2] A. K. Kerman,[3] A. Le Foll,[1,*] N. C. Luhmann, Jr.,[2] and B. Rupp[4]
[1]*Institute for Laser Science and Applications, Lawrence Livermore National Laboratory, Livermore, California 94550*
[2]*Department of Applied Science, University of California, Davis, California 95616*
[3]*Center for Theoretical Physics and Physics Department, Massachusetts Institute of Technology, Cambridge, Massachusetts 02139*
[4]*Biology and Biotechnology Research Program, Lawrence Livermore National Laboratory, Livermore, California 94550*
(Received 18 September 2000; revised manuscript received 26 February 2001; published 15 June 2001)

A complete, three-dimensional theory of Compton scattering is described, which fully takes into account the effects of the electron beam emittance and energy spread upon the scattered x-ray spectral brightness. The radiation scattered by an electron subjected to an arbitrary electromagnetic field distribution in vacuum is first derived in the linear regime, and in the absence of radiative corrections; it is found that each vacuum eigenmode gives rise to a single Doppler-shifted classical dipole excitation. This formalism is then applied to Compton scattering in a three-dimensional laser focus, and yields a complete description of the influence of the electron beam phase-space topology on the x-ray spectral brightness; analytical expressions including the effects of emittance and energy spread are also obtained in the one-dimensional limit. Within this framework, the x-ray brightness generated by a 25 MeV electron beam is modeled, fully taking into account the beam emittance and energy spread, as well as the three-dimensional nature of the laser focus; its application to x-ray protein crystallography is outlined. Finally, coherence, harmonics, and radiative corrections are also briefly discussed.

DOI: 10.1103/PhysRevE.64.016501 PACS number(s): 41.60.−m, 42.50.Ar, 41.75.Ht, 52.38.−r

I. GENERAL CONSIDERATIONS

Remarkable advances in ultrashort-pulse laser technology based on chirped-pulse amplification [1–4], and the recent development of high-brightness, relativistic electron sources [5–7] allow the design of novel, compact, monochromatic, tunable, femtosecond x-ray sources using Compton scattering [8–21]. Such new light sources are expected to have a major impact in a number of important fields of research, including the study of fast structural dynamics [22–24], advanced biomedical imaging [25,26], and x-ray protein crystallography [27,28]; however, the quality of both the electron and laser beams is of paramount importance in achieving the peak and average x-ray spectral brightness required for such applications. One of the primary purposes of this paper is therefore to establish a theoretical formalism capable of fully describing the three-dimensional nature of the interaction, as well as the influence of the electron and laser beam phase space topologies upon the x-ray spectral brightness. To our knowledge, this is the first detailed analysis of its kind; furthermore, the radiation theorem that is demonstrated and used in this work is of a general nature, and is hoped to represent a useful contribution to the field of classical electrodynamics; finally, analytical expressions of the x-ray spectral brightness including the effects of emittance and energy spread are obtained in the one-dimensional limit.

The aforementioned technical breakthroughs in the fields of solid-state lasers and high-brightness electron accelerators provide a unique opportunity to develop an entirely new class of advanced x-ray sources, with characteristics approaching those of third-generation light sources [29], in a much more compact and inexpensive package. This, in turn, offers the possibility of an important spin-off of ultrashort-pulse laser technology into the field of molecular biology, which is currently growing at an exponential rate: following the completion of the Human Genome Project [30], the systematic study of protein structure and function [31,32] is expected to dominate biophysics in the first half of the 21st century. In addition, a new paradigm for rational drug design has now emerged, using both recombinant DNA technology [33] and x-ray protein crystallography. New classes of drugs [34], as recently exemplified by the development of HIV protease inhibitors [35,36], successfully reduced the viral load of AIDS patients below the detection threshold of enzyme-linked immunosorbent assays [37].

In protein crystallography, recombinant DNA technology is used to produce large quantities of a given protein by splicing the corresponding coding DNA sequence into the genetic material of a bacterium. The transfected bacteria are cultivated and, upon induction, overexpress large quantities of the selected protein, which is then isolated, purified, and crystallized. Diffraction data are routinely collected at LN_2 temperature, and the experimental phase measurements necessary for the reconstruction of the electron density are primarily determined by the multiwavelength anomalous diffraction (MAD) method [27,28,38]. Finally, a molecular model of the structure is built into the reconstructed three-dimensional electron density map.

The key characteristics of an x-ray source useful for protein crystallography are its small size, low angular divergence, good transverse coherence, and high average spectral brightness. In turn, these requirements determine the necessary electron and laser beam quality, as will be discussed extensively in this paper.

This paper is organized as follows: in Sec. II, a radiation theorem is demonstrated, which enables us to derive the ra-

*Permanent address: Ecole Polytechnique, 91128 Palaiseau, France.

 ©2001 The American Physical Society

diation of an electron subjected to an arbitrary electromagnetic field distribution in vacuum, provided that the maximum vector potential characterizing the field satisfies the condition $eA/m_0c \ll 1$, and that radiative corrections can be neglected [20,21,39]; in Sec. III, this theorem is used in the one-dimensional, plane-wave limit to obtain analytical expressions of the effects of energy spread and emittance upon the scattered x-ray spectral brightness; in Sec. IV, the three-dimensional theory is developed, and an analytical expression of the spectral brightness is obtained within the context of the paraxial approximation [40,41]; in Sec. V, the architecture of the three-dimensional Compton scattering code is outlined, and detailed simulations are performed in the case of a 25-MeV electron beam scattering x rays near 1 Å; finally, in Sec. VI, a cursory overview of one of the main applications targeted for the advanced Compton light source, x-ray protein crystallography, is given, as well as a brief description of our micro-MAD (μMAD) concept; conclusions are drawn in Sec. VII. Coherence [42], harmonic production [16–21], and radiative corrections [20,21] are briefly discussed in the Appendix.

II. RADIATION THEOREM

Our first task is to demonstrate the following theorem: in the linear regime, where the 4-potential amplitude satisfies the condition $eA/m_0c \ll 1$, and in the absence of radiative corrections [20,21,39], where the frequency cutoff is $\omega \ll m_0c^2/\hbar$, as measured in the electron frame, the spectral photon number density scattered by an electron interacting with an *arbitrary* electromagnetic field distribution *in vacuum* is given by the momentum space distribution of the incident vector potential at the Doppler-shifted frequency:

$$\frac{d^2N_x(k_\mu^s)}{d\omega_s d\Omega} = \frac{\alpha}{(2\pi)^4}\frac{1}{\gamma_0^2\omega_s}\left|\mathbf{k}_s \times \int_{\mathbb{R}^3}\left[1+\left(\frac{\mathbf{k}}{\kappa_s}\right)\mathbf{u}_0\cdot\right]\tilde{\mathbf{A}} \times\left[\omega_s - \frac{\mathbf{u}_0}{\gamma_0}\cdot(\mathbf{k}_s-\mathbf{k}),\mathbf{k}\right]\exp(i\mathbf{k}\cdot\mathbf{x}_0)d^3\mathbf{k}\right|^2. \tag{1}$$

Here, $k_\mu^s = (\omega_s, \mathbf{k}_s) = \omega_s(1,\hat{\mathbf{n}})$ is the 4-wave-number of the wave scattered in the observation direction $\hat{\mathbf{n}}$, at the frequency ω_s; $\alpha = e^2/2\varepsilon_0 hc \simeq 1/137.036$ is the fine-structure constant; $u_\mu^0 = (\gamma_0, \mathbf{u}_0)$ is the electron initial 4-velocity; $x_\mu^0 = (0,\mathbf{x}_0)$ is its initial 4-position; and we have introduced the scattered light-cone variable, $\kappa_s = -u_0^\mu k_\mu^s = \gamma_0\omega_s - \mathbf{u}_0\cdot\mathbf{k}_s$. The term $[1+(\mathbf{k}/\kappa_s)\mathbf{u}_0\cdot]$ is to be considered as an operator acting on the Fourier transform of the spatial components of the 4-potential, $A_\mu = (\mathcal{V},\mathbf{A})$,

$$\tilde{A}_\mu(k_\nu) = \frac{1}{(\sqrt{2\pi})^4}\int_{\mathbb{R}^4} A_\mu(x^\nu)\exp(ik_\nu x^\nu)d^4k_\nu, \tag{2}$$

while the term $\exp(i\mathbf{k}\cdot\mathbf{x}_0)$ will be shown to give rise to the coherence factor [42,43]. This theorem is then applied to the specific case of Compton scattering [15–21] in a three-dimensional Gaussian-elliptical focus [40,41]. The effects of the electron beam phase-space topology are also included, in the form of energy spread and emittance [44–46].

In our analysis, charge is measured in units of e, mass in units of m_0, length is normalized to a reference wavelength k_0^{-1}, while time is measured in units of the corresponding frequency, $\omega_0^{-1} = (ck_0)^{-1}$. Neglecting radiative corrections [20,21,39], the electron motion is governed by the Lorentz force equation $du_\mu/d\tau = -(\partial_\mu A_\nu - \partial_\nu A_\mu)u^\nu$. Here, $u_\mu = dx_\mu/d\tau$ is the electron 4-velocity along its world line $x_\mu(\tau)$; τ is the electron proper time; A_μ is the 4-potential from which the electromagnetic field derives; finally, $\partial_\mu = (-\partial_t, \nabla)$ is the 4-gradient operator [47,48]. The electromagnetic field distribution considered here corresponds to a vacuum interaction; therefore, the 4-potential satisfies the wave equation, $\Box A_\mu = [\partial_\nu\partial^\nu]A_\mu = \emptyset$, and can be expressed as a superposition of plane waves, as described in Eq. (2). Furthermore, we choose to work in the Lorentz gauge, where $\partial_\mu A^\mu = 0$. Here, the symbol $\emptyset = (0,\mathbf{0})$ represents the null 4-vector.

A. Covariant linearization

Introducing the maximum amplitude of the 4-potential, A, we can linearize the Lorentz force equation, provided that $A \ll 1$, a condition that is typically satisfied in most experimental situations: for example, in the case of an ultrahigh-intensity laser focus, this condition translates into a maximum intensity below 10^{17} W/cm^2 for visible wavelengths. We then write $u_\mu = u_\mu^0 + u_\mu^1 + u_\mu^2 + \cdots$, where $u_\mu^n \propto A^n$, and the Lorentz force equation yields, to first order,

$$\frac{du_\mu^1}{d\tau} \simeq -(\partial_\mu A_\nu - \partial_\nu A_\mu)u_0^\nu. \tag{3}$$

To solve Eq. (3), we Fourier transform the first-order 4-velocity perturbation into momentum space:

$$u_\mu^1(x^\nu) = \frac{1}{(\sqrt{2\pi})^4}\int_{\mathbb{R}^4} d^4k_\nu \tilde{u}_\mu^1(k_\nu)\exp(ik_\nu x^\nu); \tag{4}$$

because of the orthogonality of complex exponentials, Eq. (3) takes the form

$$\tilde{u}_\mu^1 ik_\nu \frac{dx^\nu}{d\tau} \simeq -u_0^\nu(ik_\mu\tilde{A}_\nu - ik_\nu\tilde{A}_\mu), \tag{5}$$

and the term $dx^\nu/d\tau = u^\nu$ must be approximated by u_0^ν within the context of the linear theory presented here; we then find that $\tilde{u}_\mu^1 \simeq \tilde{A}_\mu - k_\mu\tilde{A}_\nu u_0^\nu/k_\nu u_0^\nu$.

Fourier transforming this result back into space-time, we finally obtain

$$u_\mu(x^\nu) \simeq u_\mu^0 + \frac{1}{(\sqrt{2\pi})^4}\int_{\mathbb{R}^4} d^4k_\nu \times\left[\tilde{A}_\mu(k_\nu) - k_\mu\frac{\tilde{A}_\nu(k_\nu)u_0^\nu}{k_\nu u_0^\nu}\right]\exp(ik_\nu x^\nu). \tag{6}$$

The linearization procedure used here is manifestly covariant.

B. Nonlinear plane-wave dynamics

It is interesting to compare the result given in Eq. (6) with the full nonlinear theory in the case of a single plane-wave electromagnetic eigenmode in vacuum, where the 4-potential is an arbitrary function of the relativistically invariant phase: $A_\mu(x^\nu)=A_\mu(\phi)$, $\phi(x^\nu)=-k_\nu x^\nu$. In this case, the operation of the 4-gradient upon the 4-potential reduces to

$$\partial_\mu A_\nu=\frac{\partial\phi}{\partial x^\mu}\frac{dA_\nu}{d\phi}=-k_\mu\frac{dA_\nu}{d\phi}. \tag{7}$$

Applying this result to the Lorentz force equation, we have

$$\frac{du_\mu}{d\tau}=k_\mu\left(u^\nu\frac{dA_\nu}{d\phi}\right)-(k_\nu u^\nu)\frac{dA_\mu}{d\phi}=k_\mu\left(u^\nu\frac{dA_\nu}{d\phi}\right)+\frac{d\phi}{d\tau}\frac{dA_\mu}{d\phi}$$
$$=\frac{dA_\mu}{d\tau}+k_\mu\left(u^\nu\frac{dA_\nu}{d\phi}\right); \tag{8}$$

here, we recognize the canonical momentum, $\pi_\mu=u_\mu-A_\mu$ [49]. We now consider the light-cone variable, $\kappa=d\phi/d\tau$; the evolution of this dynamical variable is described by

$$\frac{d\kappa}{d\tau}=-k_\mu\frac{du^\mu}{d\tau}=-k_\mu\left(k^\mu\frac{dA^\nu}{d\phi}-k^\nu\frac{dA^\mu}{d\phi}\right)u_\nu$$
$$=-(k_\mu k^\mu)\left(\frac{dA^\nu}{d\phi}u_\nu\right)+(k^\nu u_\nu)\left(k_\mu\frac{dA^\mu}{d\phi}\right). \tag{9}$$

The first term in Eq. (9) corresponds to the mass-shell condition, $k_\mu k^\mu=0$, and can easily be derived by considering the propagation equation in vacuum,

$$\Box A_\mu=(\partial_\nu\partial^\nu)A_\mu=0=\frac{\partial\phi}{\partial x^\nu}\frac{\partial\phi}{\partial x_\nu}\frac{d^2A_\mu}{d\phi^2}=(k_\nu k^\nu)\frac{d^2A_\mu}{d\phi^2}; \tag{10}$$

while the second term in Eq. (9) corresponds to the Lorentz gauge condition [47,48,50],

$$\partial_\mu A^\mu=0=\frac{\partial\phi}{\partial x^\mu}\frac{dA^\mu}{d\phi}=-k_\mu\frac{dA^\mu}{d\phi}. \tag{11}$$

With this, we see that the light-cone variable is a constant of the electron motion:

$$\frac{d\kappa}{d\tau}=0.$$

We now return to Eq. (8): from its structure, we can see that the solution must take the form $u_\mu=A_\mu+k_\mu g(\phi)$, where g is a function of the electron phase to be determined; in addition, the nonlinear radiation pressure of the plane wave is proportional to $A_\mu A^\mu(\phi)$: finally, the solution must satisfy the condition $u^\mu u_\mu=-1$. Therefore, we consider

$$u_\mu=A_\mu+k_\mu\left[\frac{\zeta+A_\nu A^\nu}{2\kappa}\right], \tag{12}$$

which has the appropriate structure, and where ζ is a constant that will be determined from the normalization of the 4-velocity. Deriving the trial solution with respect to proper time, we first have

$$\frac{du_\mu}{d\tau}=\frac{dA_\mu}{d\tau}+\frac{k_\mu}{2\kappa}\left(2A_\nu\frac{dA^\nu}{d\tau}\right)=\frac{dA_\mu}{d\tau}+\frac{k_\mu}{\kappa}\left(A_\nu\frac{dA^\nu}{d\phi}\frac{d\phi}{d\tau}\right)$$
$$=\frac{dA_\mu}{d\tau}+k_\mu\left(A_\nu\frac{dA^\nu}{d\phi}\right); \tag{13}$$

we then use Eq. (12) to replace the 4-potential

$$A_\nu=u_\nu-k_\nu\left[\frac{\zeta+A_\lambda A^\lambda}{2\kappa}\right],$$

and we find that

$$\frac{du_\mu}{d\tau}=\frac{dA_\mu}{d\tau}+k_\mu\left(u_\nu\frac{dA^\nu}{d\tau}\right)-k_\mu\left[\frac{\zeta+A_\lambda A^\lambda}{2\kappa}\right]\left(k_\nu\frac{dA^\nu}{d\tau}\right), \tag{14}$$

which reduces exactly to the Lorentz force equation because the Lorentz gauge condition requires that $k_\nu dA^\nu/d\tau=0$, as shown in Eq. (11). In turn, the structure of the solution given in Eq. (12) implies that the light-cone variable reduces to

$$\kappa=-k_\mu u^\mu=-k_\mu A^\mu-(k_\mu k^\mu)\left[\frac{\zeta+A_\nu A^\nu}{2\kappa}\right]=-k_\mu A^\mu, \tag{15}$$

because of the mass-shell condition, $k_\mu k^\mu=0$; we can also verify that the light-cone variable is, indeed, constant:

$$\frac{d\kappa}{d\tau}=-k_\mu\frac{dA^\mu}{d\tau}=-\left(k_\mu\frac{dA^\mu}{d\phi}\right)\frac{d\phi}{d\tau}=0,$$

because of the Lorentz gauge condition. Using Eq. (15), we can now rewrite the 4-velocity as

$$u_\mu=A_\mu-k_\mu\left[\frac{\zeta+(A_\nu A^\nu)}{2k_\nu A^\nu}\right];$$

finally, the constant ζ is determined by taking the norm of the 4-velocity:

$$u_\mu u^\mu=A_\mu A^\mu-2k_\mu A^\mu\left[\frac{\zeta+(A_\nu A^\nu)}{2k_\nu A^\nu}\right]+(k_\mu k^\mu)\left[\frac{\zeta+(A_\nu A^\nu)}{2k_\nu A^\nu}\right]^2$$
$$=-\zeta$$
$$=-1, \tag{16}$$

where we have used the mass-shell condition again. Thus, the fully covariant, nonlinear solution to the electron dynamics in a plane wave of arbitrary intensity and temporal dependence is found to be

$$u_\mu(x^\nu)=u_\mu(\phi)=A_\mu-k_\mu\left(\frac{1+A_\nu A^\nu}{2k_\nu A^\nu}\right). \tag{17}$$

The question of the influence of the initial conditions on the electron trajectory can now be addressed: the 4-potential can be regauged to incorporate the boundary conditions on the electron dynamics. Since we are shifting the 4-potential by a constant 4-vector, the Lorentz gauge condition is still satisfied and the electromagnetic field tensor is unchanged; we have $A^\mu\to A^\mu+u_0^\mu$, $\lim_{\phi\to\infty}A^\mu(\phi)=0$, $\lim_{\phi\to\infty}u^\mu(\phi)=u_0^\mu$. With this, the invariant light-cone variable reads $\kappa=-k_\mu A^\mu=-k_\mu u_0^\mu$, and the 4-velocity is given by

$$u^\mu=u_0^\mu+A^\mu-k^\mu\left(\frac{A_\nu A^\nu+2A_\nu u_0^\nu}{2k_\nu u_0^\nu}\right), \tag{18}$$

where we have used the fact that

$$(A+u_0)_\mu(A+u_0)^\mu=A_\mu A^\mu+2A_\mu u_0^\mu-1.$$

It should be emphasized that this nonlinear solution is fully covariant and makes explicit use of gauge invariance.

The nonlinear, covariant electron dynamics are thus fully determined; the Lawson-Woodward theorem [19] is immediately recovered by considering the timelike component of Eq. (18): $\lim_{\phi\to+\infty}\gamma(\phi)=\gamma_0$, as $\lim_{\phi\to+\infty}A_\mu(\phi)=0$. In the linear regime, where the normalized 4-potential satisfies the condition $|A_\mu A^\mu|\ll 1$, the electron motion is purely transverse, while at so-called relativistic intensities, ponderomotive effects dominate [21]. In particular, the mass of the dressed electron can immediately be derived from the timelike component of Eq. (18), in a frame where the electron is initially at rest:

$$\langle m\rangle=\langle\gamma\rangle=\left\langle 1+\mathcal{V}+\frac{A_\mu A^\mu}{2}\right\rangle, \tag{19}$$

where $\mathcal{V}$ is the timelike component of the 4-potential, or scalar potential.

It is also easy to recover more familiar expressions by rotating the coordinate system so that the 4-wave-number reduces to $k_\mu=(1,0,0,1)$, and to introduce the 4-potential as $A_\mu=(0,\mathbf{A}_\perp,0)$; we then have $\kappa=\gamma-u_\parallel=\gamma_0-u_{\parallel 0}=\kappa_0$, and

$$\begin{aligned}\mathbf{u}_\perp(\phi)&=\mathbf{u}_{\perp 0}+\mathbf{A}_\perp(\phi),\\ u_\parallel(\phi)&=u_{\parallel 0}+\left[\frac{\mathbf{A}_\perp^2+2\mathbf{A}_\perp\cdot\mathbf{u}_{\perp 0}}{2(\gamma_0-u_{\parallel 0})}\right],\\ \gamma(\phi)&=\gamma_0+\left[\frac{\mathbf{A}_\perp^2+2\mathbf{A}_\perp\cdot\mathbf{u}_{\perp 0}}{2(\gamma_0-u_{\parallel 0})}\right].\end{aligned} \tag{20}$$

In particular, in the simple case where the reference frame is chosen such that $\mathbf{u}_{\perp 0}=\mathbf{0}$, we have $\gamma_0^2=1+u_{\parallel 0}^2$, and Eq. (20) reduces to the well-known result [21],

$$\mathbf{u}_\perp=\mathbf{A}_\perp,\quad u_\parallel=\gamma_0\left[\beta_{\parallel 0}+\frac{\mathbf{A}_\perp^2}{2}(1+\beta_{\parallel 0})\right],$$

$$\gamma=\gamma_0\left[1+\frac{\mathbf{A}_\perp^2}{2}(1+\beta_{\parallel 0})\right]. \tag{21}$$

Furthermore, if we linearize Eq. (18) and consider the expression of the 4-potential in momentum space, the result given in Eq. (6) becomes intuitively clear.

C. Radiation

We now consider the second half of the demonstration of the HLF theorem, as expressed in Eq. (1). The electromagnetic radiation scattered by the accelerated charge is described by the number of photons radiated per unit frequency, per unit solid angle, which is determined by Fourier transforming the electron trajectory into momentum space [51]:

$$\frac{d^2N_x(k_\mu^s)}{d\omega_s d\Omega}=\frac{\alpha\omega_s}{4\pi^2}\left|\hat{\mathbf{n}}\times\int_{-\infty}^{+\infty}\mathbf{u}(\tau)\exp[-ik_\mu^s x^\mu(\tau)]d\tau\right|^2. \tag{22}$$

Here, we have used the fact that $\hat{\mathbf{n}}$ is a unit vector to simplify the double-cross product. The spatial component of the electron 4-velocity is replaced by the linearized solution given in Eq. (6); with this, and now using the Coulomb gauge, we have

$$\begin{aligned}\frac{d^2N_x(k_\mu^s)}{d\omega_s d\Omega}=\frac{\alpha}{(4\pi^2)^3}\frac{1}{\omega_s}\Bigg|&\mathbf{k}_s\times\int_{-\infty}^{+\infty}d\tau\int_{\mathbb{R}^4}d^4k_\mu\\ &\times\left[\tilde{\mathbf{A}}(k_\mu)+\frac{\mathbf{k}}{\kappa}\mathbf{u}_0\cdot\tilde{\mathbf{A}}(k_\mu)\right]\\ &\times\exp[i(k_\mu-k_\mu^s)x^\mu(\tau)]\Bigg|^2.\end{aligned} \tag{23}$$

The electron 4-position is now approximated by $x_\mu(\tau)=x_\mu^0+u_\mu^0\tau$; this corresponds to the lowest-order convective term due to the ballistic component of the electron motion, and excludes harmonic production mechanisms (see the Appendix) [16–21]; this approximation is valid for high-Doppler-shift scattering, where the transverse oscillation scale is given by $A\lambda_0/\gamma_0\ll\lambda_0$. Using the light-cone variables, κ and κ_s, we find that

$$\begin{aligned}\frac{d^2N_x(k_\mu^s)}{d\omega_s d\Omega}=\frac{\alpha}{(4\pi^2)^3}\frac{1}{\omega_s}\Bigg|&\mathbf{k}_s\times\int_{\mathbb{R}^4}d^4k_\mu\left(\tilde{\mathbf{A}}+\frac{\mathbf{k}}{\kappa}\mathbf{u}_0\cdot\tilde{\mathbf{A}}\right)\\ &\times\exp[i(k_\mu-k_\mu^s)x_0^\mu]\int_{-\infty}^{+\infty}d\tau\exp[i(\kappa-\kappa_s)\tau]\Bigg|.\end{aligned} \tag{24}$$

The integral over proper time yields a δ-function:

$$\int_{-\infty}^{+\infty}d\tau\exp[i(\kappa-\kappa_s)\tau]=2\pi\delta(\kappa-\kappa_s).$$

We now perform the change of variable $d^4k_\mu=|\partial q_\nu/\partial k_\mu|^{-1}d^4q_\nu$, where we have introduced the four-vector

$$q_\nu = [\kappa(k_\mu), \mathbf{k}] = (u_0^\mu k_\mu, \mathbf{k}) = (\gamma_0 \omega - \mathbf{u}_0 \cdot \mathbf{k}, \mathbf{k}),$$

which allows us to perform the integral over the δ function; we then find that the Doppler condition derives from the equality of $\kappa_s = -u_0^\mu k_\mu^s = \gamma_0 \omega_s - \mathbf{u}_0 \cdot \mathbf{k}_s$, and $\kappa = -u_0^\mu k_\mu = \gamma_0 \omega - \mathbf{u}_0 \cdot \mathbf{k}$: this yields the well-known Compton scattering relation $\omega_s = (\gamma_0 \omega - \mathbf{u}_0 \cdot \mathbf{k})/(\gamma_0 - \mathbf{u}_0 \cdot \hat{\mathbf{n}})$, in the limit where recoil is negligible. Finally, using the Jacobian of the transform, $|\partial q_\nu / \partial k_\mu|^{-1} = \gamma_0^{-1}$, we obtain the sought-after result, as presented in the HLF theorem.

III. ONE-DIMENSIONAL THEORY OF EMITTANCE IN COMPTON SCATTERING

To demonstrate the usefulness of the HLF theorem, we first consider the case of a linearly polarized plane wave with an arbitrary temporal profile: the 4-potential is $A_\mu(\phi) = \hat{\mathbf{x}} A_0 g(\phi) e^{-i\phi}$, where $\phi = -k_\mu^0 x^\mu$, and $k_\mu^0 = (1,0,0,1)$, for a wave propagating along the z axis. Introducing the temporal Fourier transform of the pulse envelope, $\tilde{g}(\omega) = \int_{-\infty}^{+\infty} g(t) e^{-i\omega t} dt / \sqrt{2\pi}$, we have

$$\tilde{A}_\mu(k_\nu) = \hat{\mathbf{x}} (\sqrt{2\pi})^3 A_0 \delta(k_x) \delta(kg) \delta(\omega - k_z) \tilde{g}(1-\omega), \tag{25}$$

where $\delta(\omega - k_z)$ corresponds to the pulse propagation, and $\tilde{g}(1-\omega)$ is the spectrum of the pulse, centered around the normalized frequency, $\omega_0 = 1$, in our units. Applying the HLF theorem, we immediately find

$$\frac{d^2 N_x}{d\omega_s d\Omega} = \frac{\alpha}{2\pi} \omega_s \frac{A_0^2}{\kappa_0^2} \left| \hat{\mathbf{n}} \times \left(\hat{\mathbf{x}} + \frac{u_{0x}}{\kappa_0} \hat{\mathbf{z}} \right) \right|^2 \tilde{g}^2 \left(1 - \frac{\kappa_0^s}{\kappa_0} \right), \tag{26}$$

where $\kappa_0 = \gamma_0 - \mathbf{u}_0 \cdot \hat{\mathbf{z}} = \gamma_0 - u_{0z}$, and $\kappa_0^s = \omega_s (\gamma_0 - \mathbf{u}_0 \cdot \hat{\mathbf{n}})$. Introducing the normalized Doppler-shifted frequency $\chi = \kappa_0^s / \kappa_0 = \omega_s (\gamma_0 - \mathbf{u}_0 \cdot \hat{\mathbf{n}})/(\gamma_0 - u_{0z})$, and the differential scattering cross section, or radiation pattern,

$$\mathscr{I} = \left| \frac{\hat{\mathbf{n}} \times (\kappa_0 \hat{\mathbf{x}}_0 + u_{0x} \hat{\mathbf{z}})}{\kappa_0^2} \right|^2,$$

this result can be recast as

$$\frac{d^2 N_x}{d\omega_s d\Omega} = \frac{\alpha}{2\pi} A_0^2 \omega_s \mathscr{I} \tilde{g}^2 (1-\chi). \tag{27}$$

A. The one-dimensional cold spectral density

In the case of a Gaussian pulse envelope, where $g(t) = e^{-t^2/\Delta t^2}$, and for the interaction geometry shown in Fig. 1, Eq. (27) takes the familiar form

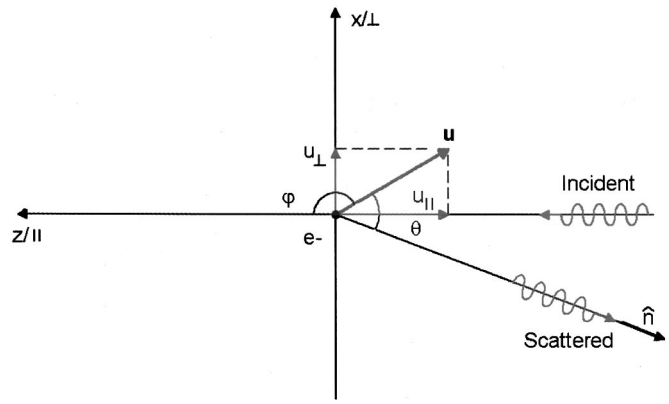

FIG. 1. Schematic of the three-dimensional Compton scattering geometry.

$$\frac{d^2 N_x}{d\omega_s d\Omega} = \frac{\alpha}{4\pi} A_0^2 \Delta\phi^2 \omega_s \times \exp\left\{ -\frac{\Delta\phi^2}{2} [\chi(\omega_s, \gamma_0, \theta, \varphi) - 1]^2 \right\} \times \frac{[\gamma_0 \cos(\theta + \varphi) - u_0 \cos\theta]^2}{[\gamma_0 - u_0 \cos\varphi]^4}. \tag{28}$$

Here, φ is the incidence angle between the initial electron velocity and the direction of propagation of the plane wave, and θ is the scattering angle, measured with respect to the electron initial velocity. Equation (28) clearly shows that the scattering spectral density is proportional to the incident photon number density, as represented by the laser intensity $A_0^2 \Delta\phi$, and that the cold spectral bandwidth of the x rays is given by that of the incident laser pulse, $\Delta\phi^{-1} = 1/\omega_0 \Delta t$. Equation (28) also indicates that the peak intensity is radiated near the Doppler-shifted frequency, where $\chi(\omega_x, \gamma_0, \theta, \varphi) \simeq 1$; this yields $\hbar\omega_x(\gamma_0, \theta, \varphi) = \hbar\omega_0(\gamma_0 - u_0 \cos\varphi)/(\gamma_0 - u_0 \cos\theta)$. For a head-on collision, where $\varphi = \pi$, the frequency radiated on axis, for $\theta = 0$, is the same as the free-electron laser (FEL) frequency for an electromagnetic wiggler [52]: for ultrarelativistic (UR) electrons, we recover the well-known relation, $\omega_x = \gamma^2 (1+\beta)^2 \simeq 4\gamma^2$.

For a number of radiating electrons N_e, the various initial positions must be taken into account, as the coherence factor [42,43] now appears as a sum of phasors: $|\Sigma_{n=1}^{N_e} \exp(i\mathbf{k} \cdot \mathbf{x}_{0n})|^2$; this forms the basis of the stochastic electron gas (SEG) theory of coherence in Compton scattering [42], which is briefly presented in the Appendix. Here, incoherent summations over the electron beam phase-space distribution will be used to study the influence of the phase-space topology on the scattered radiation.

The angular x-ray energy distribution can be mapped by considering the position of the spectral peak, where $\omega_s = \omega_x$, and $\chi = 1$. We then find that

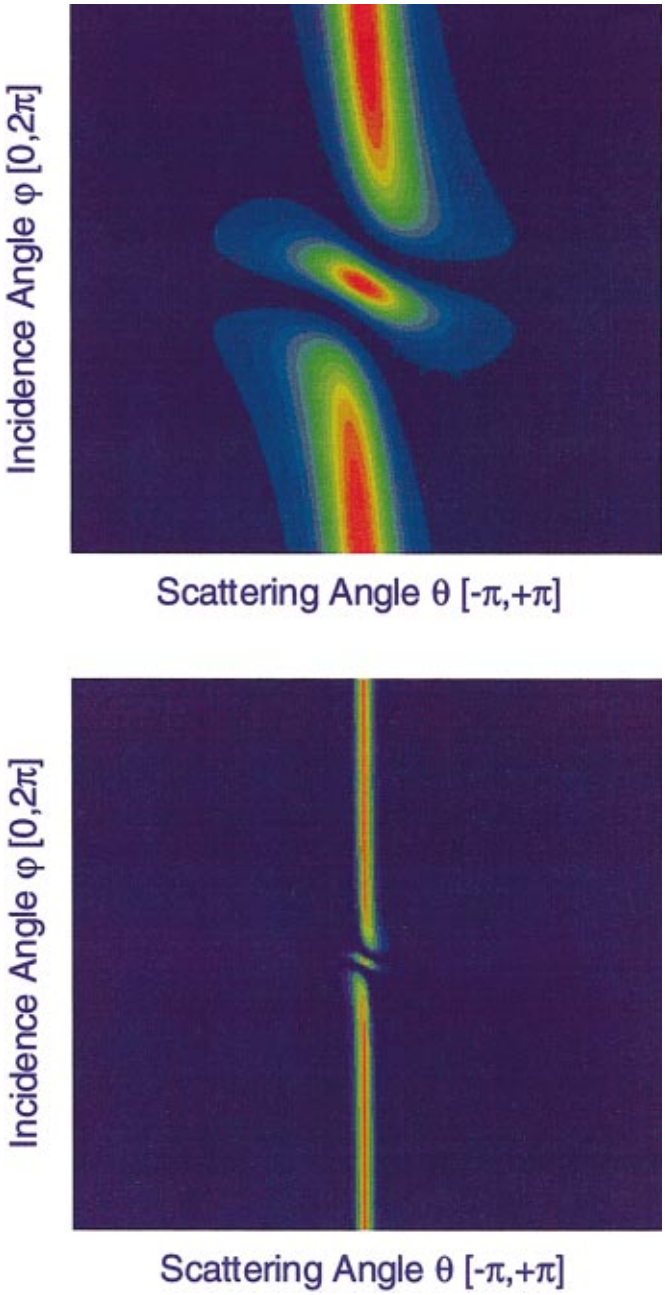

FIG. 2. (Color) Angular x-ray distribution, $[\{\gamma\cos(\varphi+\theta)-u\cos\theta\}/(\gamma-u\cos\theta)(\gamma-u\cos\varphi)]^2$, for $\gamma=2$ (top) and $\gamma=10$ (bottom).

$$\frac{d^2N_x}{d\omega\, d\Omega}(\omega_x,\hat{\mathbf{n}}) = \frac{\alpha}{4\pi}A_0^2\Delta\phi^2\frac{[\gamma\cos(\varphi+\theta)-u(\gamma)\cos\theta]^2}{[\gamma-u(\gamma)\cos\theta][\gamma-u(\gamma)\cos\varphi]^3}; \tag{29}$$

in the particular case of a head-on collision ($\varphi=\pi$), the angular behavior reduces to

$$\frac{\cos^2\theta}{[\gamma-u(\gamma)\cos\theta][\gamma+u(\gamma)]}\approx\frac{\gamma-u(\gamma)}{\gamma-u(\gamma)\cos\theta}, \tag{30}$$

where the approximation holds for small angles; the full width at half maximum (FWHM) of the x-ray cone can be derived by further simplifying Eq. (30) for UR electrons and small angles, where we can use the following approximations: $u(\gamma)\simeq\gamma-(1/2\gamma)$, and $\cos\theta=1-\theta^2/2$, respectively. With this, the angular energy distribution is described by a Lorentzian: $1/[1+(\gamma\theta)^2]$, which has an angular FWHM equal to $2/\gamma$. This well-known behavior of the x-ray frequency-integrated cone [29] is illustrated in Fig. 2

Before studying the effect of energy spread and emittance [44–46], we also note that the cold, average on-axis brightness of the x-ray source can be estimated by multiplying the spectral brightness by the normalized average electron bunch current $\langle I_b\rangle=q\rho$, where ρ is the repetition rate of the system; by considering a 1-mrad^2 solid angle, $\Delta\Omega=10^{-6}$, and a 0.1% fractional bandwidth, $\Delta\omega=\omega_x\times10^{-3}$; and by normalizing the source size to 1 mm^2; with this we obtain

$$\langle B_x\rangle=\frac{\alpha}{4\pi}\frac{\langle I_b\rangle}{\pi r_b^2}A_0^2\Delta\phi^2\omega_x\times10^{-15}, \tag{31}$$

where $\langle B_x\rangle$ is expressed in units of photons per 0.1% bandwidth, per mrad^2, per mm^2, per s, and r_b is the electron-beam spot size, which we assume to be equal to the laser spot size. The normalized vector potential is given by

$$A_0=\frac{e}{\omega_0 m_0 c}\left(\frac{2}{\varepsilon_0 c}\frac{\mathscr{W}_0}{\pi w_0^2\Delta t}\right)^{1/2}$$

as expressed in terms of the laser pulse energy $\mathscr{W}_0$, duration Δt, frequency ω_0, and focal spot size w_0. With this, the main scaling laws for the x-ray brightness are clearly exhibited: bilinear in the laser pulse energy and electron bunch charge, and inversely proportional to the fourth power of the source size, $1/w_0^2r_b^2$.

B. Energy spread

The formalism used to model the influence of the electron beam phase-space topology is now illustrated in the case of a linearly polarized plane wave with an arbitrary temporal profile; in this simple case, analytical results are derived. We introduce the cold, one-dimensional spectral brightness,

$$S_0(\omega,\gamma,\phi,\varphi)=\frac{4\pi}{\alpha A_0^2\Delta\phi^2}\frac{d^2N_x}{d\omega\, d\Omega} =\omega\exp\left\{-\frac{\Delta\phi^2}{2}[\chi(\omega,\gamma,\theta,\varphi)-1]^2\right\} \times\mathscr{I}(\gamma,\theta,\varphi). \tag{32}$$

Note that as S_0 is a function of the electron initial energy γ, scattering angle θ, and incident angle φ, we can perform incoherent summations over the electron initial energy and momentum distributions to study the effects of energy spread and emittance. For conciseness, the scattered frequency is now labeled as ω, and the initial electron 4-velocity is labeled as $u_\mu^0=(\gamma,\mathbf{u})$, where $u=\sqrt{\gamma^2-1}$. The use of incoher-

ent summations, while intuitively obvious, will be rigorously justified *a posteriori* in the Appendix.

We start with the beam energy spread; the ''warm'' beam brightness is given by

$$S_\gamma(\omega,\gamma_0,\Delta\gamma,\theta,\varphi)$$

$$= \frac{1}{\sqrt{\pi}\Delta\gamma}\int_1^\infty S_0(\omega,\gamma,\theta,\varphi)\exp\left[-\left(\frac{\gamma-\gamma_0}{\Delta\gamma}\right)^2\right]d\gamma,$$

$$\simeq \frac{\omega\mathscr{f}(\gamma_0,\theta,\varphi)\exp\left(\frac{\mathscr{u}^2}{\mathscr{v}}-\mathscr{w}\right)}{\left\{1+\frac{1}{2}\left(\Delta\phi\frac{\Delta\gamma}{\gamma_0}\right)^2\left[\frac{\omega}{\gamma_0^2}\frac{\cos\varphi-\cos\theta}{(1-\cos\varphi)^2}\right]^2\right\}^{1/2}}, \tag{33}$$

where we have used a Gaussian distribution to model the beam longitudinal phase space. Note that as

$$\lim_{\Delta\gamma\to 0}\frac{1}{\sqrt{\pi}\Delta\gamma}\exp\left[-\left(\frac{\gamma-\gamma_0}{\Delta\gamma}\right)^2\right]=\delta(\gamma-\gamma_0),$$

the cold brightness is automatically recovered for a monoenergetic electron beam.

The analytical result in Eq. (33) is obtained by Taylor expanding to second order around the central electron energy γ_0. The normalization constant is given by

$$\int_1^\infty \exp\left[-\left(\frac{\gamma-\gamma_0}{\Delta\gamma}\right)^2\right]d\gamma\simeq\sqrt{\pi}\Delta\gamma, \tag{34}$$

an excellent approximation for $\gamma_0\gg 1$ and $\Delta\gamma/\gamma_0\ll 1$. Here, $\Delta\gamma$ refers to the energy spread; in addition,

$$\mathscr{a}=\frac{\omega}{\gamma_0^3}\frac{(\cos\varphi-\cos\theta)}{(1-\cos\varphi)^2},\quad \mathscr{b}=\chi(\omega,\gamma_0,\theta,\varphi)-1,$$

$$\mathscr{u}=\frac{1}{\Delta\gamma^2}\left[1+\frac{\mathscr{a}}{2}(\Delta\phi\Delta\gamma)^2\right],\quad \mathscr{v}=\frac{\Delta\phi^2}{2}\mathscr{a}\mathscr{b},\quad \mathscr{w}=\frac{\Delta\phi^2}{2}\mathscr{b}^2.$$

Since $\mathscr{v}$ and $\mathscr{w}$ are both linear functions of $\mathscr{b}$, which is equal to zero at the peak of the x-ray spectrum, the exponential is equal to one for $\omega=\omega_x$. In addition, the factor $[\Delta\phi(\Delta\gamma/\gamma_0)]^2$ in the square root shows that the relative energy spread must be compared to the normalized laser pulse duration, which is equivalent to the number of electromagnetic wiggler periods; this indicates that to increase the x-ray spectral brightness by lengthening the drive laser pulse, the requirement on the electron beam energy spread becomes increasingly stringent. Figure 3 illustrates the effects of energy spread, which are seen to symmetrically broaden the scattered x-ray spectrum and lower the peak intensity; Fig. 4 shows the aforementioned saturation of the spectral brightness, as the laser pulse duration is increased, for a given value of the energy spread, and a fixed value of the normalized potential; we see that for 0.5% relative energy spread, and $\gamma_0=50$, a 200-fs laser pulse will yield the optimum spectral brightness with a minimum energy, longer pulses requiring more energy without any beneficial effects on the x-ray spectral width.

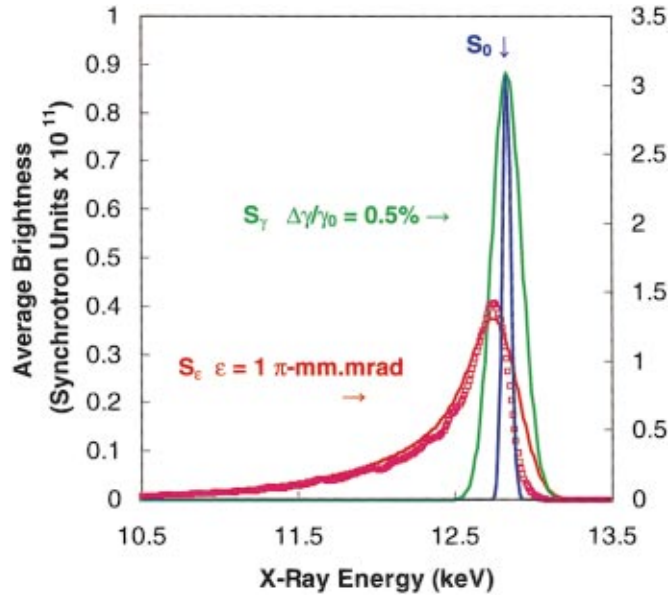

FIG. 3. (Color) On-axis x-ray spectral brightness for a cold beam (blue, right scale), $\Delta\gamma/\gamma_0=0.5\%$ (green), $\varepsilon=1$ πmm×mrad (red), and three-dimensional computer simulations (red squares). The beam energy is 22.75 MeV, the bunch charge is 0.5 nC, its duration is 1 ps; the laser wavelength is $\lambda_0=800$ nm ($TiAl_2O_3$), the laser pulse energy is 50 mJ, $w_0=r_b=10\,\mu$m cylindrical focus, $\varphi_0=180°$, $A_0=0.17$, and the overall repetition rate of the system is 1 kHz. The synchrotron units correspond to photons per 0.1% bandwidth, per mm^2, per mrad^2, per second; this is abbreviated here and in the remainder of the text as $N_x/(0.1\%\ \text{bandwidth mrad}^2\ \text{mm}^2\ \text{s})$.

C. Emittance

We now turn our attention to the influence of the electron beam emittance:

$$S_\varepsilon(\omega,\gamma_0,\Delta\gamma,\theta,\varphi_0,\Delta\varphi)\simeq\frac{1}{\sqrt{\pi}\Delta\varphi}\int_0^{2\pi}S_\gamma(\omega,\gamma_0,\Delta\gamma,\theta-\delta,\varphi_0+\delta)\exp\left[-\left(\frac{\delta}{\Delta\varphi}\right)^2\right]d\delta, \tag{35}$$

where the spread of incidence angle is given in terms of the beam emittance ε, and radius r_b, by $\Delta\varphi=\varepsilon/\gamma_0 r_b$, and where φ_0 is the mean incidence angle, defined by the laser and electron beams. Again, the normalization constant is given by

$$\int_0^{2\pi}\exp\left[-\left(\frac{\delta}{\Delta\varphi}\right)^2\right]d\delta=\sqrt{\pi}\Delta\varphi, \tag{36}$$

provided that $\Delta\varphi\ll 1$.

In Eq. (35), we note the important geometrical correction term, $\theta-\delta$, which corresponds to the fact that the scattering

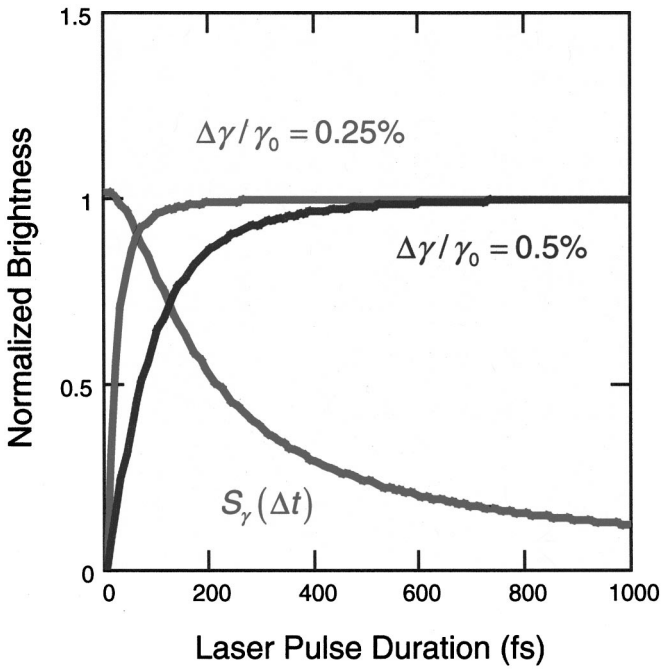

FIG. 4. On-axis x-ray spectral brightness as a function of the laser pulse duration, for two different values of the energy spread; other parameters are as in Fig. 3.

angle is measured with respect to the initial electron velocity. The effects of emittance are illustrated in Fig. 3, and are found to be independent of φ_0. Considering the on-axis x-ray spectral line, it is clear that emittance both asymmetrically broadens the spectrum and decreases the peak spectral brightness; near head-on collisions, a low-energy tail develops because the maximum Doppler-shift corresponds to $\delta=0$: other electrons produce a smaller upshift, thus contributing to the lower energy photon population as seen in Fig. 3.

Returning to the cold, one-dimensional spectral brightness, the integral over a Gaussian distribution of incidence angle can be performed analytically, provided that the spectral density is approximated by the exponential of a biquadratic polynomial [53]:

$$\int_0^\infty e^{-\mu x^4-2\nu x^2}dx=\frac{1}{4}\sqrt{2\nu/\mu}\exp\left(\frac{\nu^2}{2\mu}\right)\overline{K}_{1/4}\left(\frac{\nu^2}{2\mu}\right), \tag{37}$$

where $\overline{K}_{1/4}$ is defined in terms of Bessel functions of fractional order:

$$\overline{K}_{1/4}\left(\frac{\nu^2}{2\mu}\right)=I_{-1/4}\left(\frac{\nu^2}{2\mu}\right)-\frac{\nu}{|\nu|}I_{1/4}\left(\frac{\nu^2}{2\mu}\right). \tag{38}$$

Since $\omega\!\!\!/(\gamma,\theta,\varphi)$ is a slow-varying function of the incidence angle, we can seek an approximate expression for the cold spectral density of the form:

$$S_0(\omega,\gamma,\theta-\delta,\varphi+\delta)\simeq\omega\!\!\!/(\gamma,\theta,\varphi)\exp[-\mu(\omega,\gamma,\theta,\varphi)\delta^4-2\nu(\omega,\gamma,\theta,\varphi)\delta^2+\lambda(\omega,\gamma,\theta,\varphi)]. \tag{39}$$

The constant term is obtained by taking $\delta=0$: $\lambda(\omega,\gamma,\theta,\varphi)=-(\Delta\phi^2/2)[\chi(\omega,\gamma,\theta,\varphi)-1]^2$; the other coefficients are derived using $\cos\delta\simeq1-\delta^2/2!+\delta^2/4!$ and $\sin\delta\simeq\delta-\delta^3/3!$ We then find that $\mu=(\Delta\phi^2/2)[(\mu_1+\mu_2)/(\gamma-u\cos\varphi)]$ and $2\nu=(\Delta\phi^2/2)[(\nu_1-\nu_2)/(\gamma-u\cos\varphi)^4]$ with

$$\mu_1=(\gamma-u\cos\varphi)^2\left\{\frac{u}{12}(\cos\varphi-\cos\theta)[\gamma(\omega-1)+u(\cos\varphi-\omega\cos\theta)]-\frac{u^2}{3}(\omega\sin\theta+\sin\varphi)^2+\frac{u^2}{4}(\cos\varphi-\omega\cos\theta)^2\right\},$$

$$\mu_2=[\omega(\gamma-u\cos\theta)-\gamma+u\cos\varphi]^2\times\left[\frac{u}{12}\cos\varphi(\gamma-u\cos\varphi)+\frac{u^2}{3}\sin^2\varphi-\frac{u^2}{4}\cos^2\varphi\right],$$

$$\nu_1=(\gamma-u\cos\varphi)^2\{u^2(\omega\sin\theta+\sin\theta)^2-u(\cos\varphi-\omega\cos\theta)\times[\gamma(\omega-1)+u(\cos\varphi-\omega\cos\theta)]\},$$

$$\nu_2=[u\cos\varphi(\gamma-u\cos\varphi)+u^2\sin^2\varphi][\omega(\gamma-u\cos\theta)-(\gamma-u\cos\varphi)]^2. \tag{40}$$

This result is compared to a full three-dimensional numerical simulation on Fig. 3; the agreement is quite good. Note that to include both the effects of energy spread and emittance, the analytical results given in Eqs. (37) and (39) are multiplied by the energy spread degradation factor, as measured at the peak of the cold spectrum:

$$S_\varepsilon\simeq\frac{\omega_x\!\!\!/(\gamma_0,\theta,\varphi_0)}{\left\{1+\frac{1}{2}\left(\Delta\phi\frac{\Delta\gamma}{\gamma_0}\right)^2\left[\frac{\omega_x}{\gamma_0^2}\frac{\cos\varphi_0-\cos\theta}{(1-\cos\varphi_0)^2}\right]^2\right\}^{1/2}}\times\frac{\omega\!\!\!/(\gamma_0,\theta,\varphi_0)}{2\sqrt{\pi}\Delta\varphi}\sqrt{2\nu/\mu}\exp\left(\frac{\nu^2}{2\mu}+\lambda\right)\overline{K}_{1/4}\left(\frac{\nu^2}{2\mu}\right). \tag{41}$$

At this point, the combined effects of energy spread and emittance can be further studied by varying the bunch charge and modeling the behavior of the electron beam phase space as follows:

$$\frac{\Delta\gamma}{\gamma_0}(q)=\left\{\left[\frac{\gamma_0}{2}(\omega_{rf}\Delta\tau)^2\right]^2+\left(\frac{e}{m_0c^2}\frac{q}{2\pi\varepsilon_0c\Delta\tau}\right)^2\right\}^{1/2}, \tag{42}$$

where the first term is the spread due to the finite duration of the bunch in the rf accelerating bucket of frequency $\omega_{rf}/2\pi$,

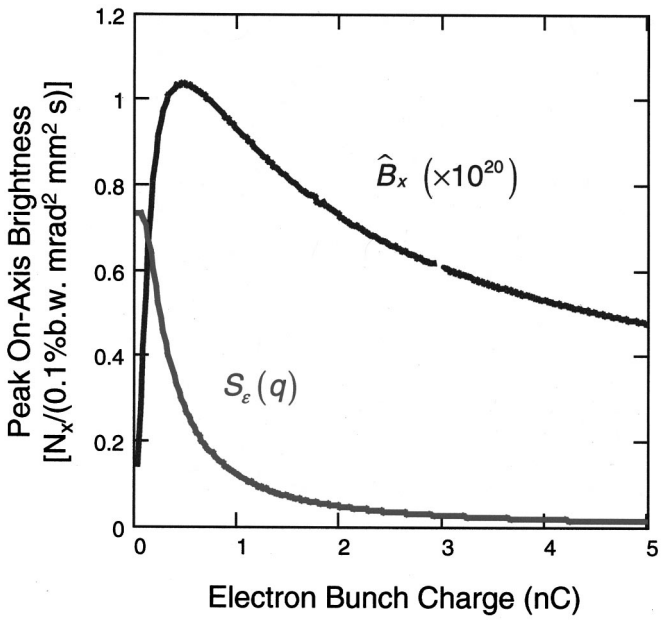

FIG. 5. On-axis x-ray brightness as a function of the electron bunch charge; all other parameters are as in Fig. 3. $S_\varepsilon(q)$ is dimensionless.

while the second term corresponds to space-charge; for the emittance, an empirical linear scaling with charge is chosen [54], with $\varepsilon(q)\simeq\sigma q$, and $\sigma=1\pi$ mm×mrad/nC. This results in the brightness curve shown in Fig. 5, where the brightness first scales linearly with the charge, reaches a maximum near 0.5 nC, and starts degrading thereafter under the combined influences of energy spread and emittance. This optimum value of the charge is quite interesting as it very nearly corresponds to the state-of-the-art for high-brightness photoinjectors [5–7].

IV. THREE-DIMENSIONAL THEORY OF EMITTANCE IN COMPTON SCATTERING

The HLF theorem is now applied to the case of a three-dimensional laser focus. The transverse laser profile is specified at the focal plane, and propagated using the method discussed in Ref. [40] where the vector potential derives from a generating function: $\mathbf{A}=\boldsymbol{\nabla}\times\mathbf{G}$; in this manner, the Coulomb gauge condition, $\boldsymbol{\nabla}\cdot\mathbf{A}=0$, is automatically satisfied. For a linearly polarized Gaussian-elliptical focus, with focal waists w_{0x} and w_{0y}, and a monochromatic wave at the central frequency $\omega_0=1$, with a Gaussian envelope of duration $\omega_0\Delta t=\Delta\phi$, the 4-potential is represented in momentum-space by

$$\tilde{A}_\mu(k_\nu)=\frac{\sqrt{\pi}}{2}A_0 w_{0x}w_{0y}\Delta t \times\exp\left\{-\left[\frac{w_{0x}k_x}{2}\right]^2-\left[\frac{w_{0y}k_y}{2}\right]^2-\left[\frac{\Delta t(\omega-1)}{2}\right]^2\right\} \times\delta(k_z-\sqrt{\omega^2-k_x^2-k_y^2})[i(-\hat{\mathbf{x}}k_z+\hat{\mathbf{z}}k_x)]. \tag{43}$$

Here, we recognize the $\mathbf{k}_\perp$ spectrum, the frequency spectrum, the propagator, $\delta(k_\mu k^\mu)$, and the curl operator, as expressed in momentum space.

The scattered radiation can now be determined by using the HLF theorem; to obtain an analytical result than can be further exploited to include the phase-space topology of the electron beam interacting with the laser pulse using the method outlined above, the paraxial propagator formalism [40,41] is used: the phase function $\delta(k_z-\sqrt{\omega^2-k_x^2-k_y^2})$, is replaced by $\delta[k_z-\omega+(k_x^2/2k_0)+(k_y^2/2k_0)]$. The accuracy of the paraxial approximation has been studied in detail [40,41], and found to be extremely good over a wide range of parameters; however, in the case of Compton scattering, the following conditions must also be satisfied: $\kappa_0^2 w_{0,x,y}^2 > \Delta\phi^2[u_z(\kappa_s-\kappa_0)-u_{x,y}^2]$.

With this proviso, the integrals over the transverse wave number components converge, and can be performed analytically [53]: we use the well-known integral of the exponential of a complex, second-order polynomial,

$$\int_{-\infty}^{+\infty} e^{-(ax^2+2bx+c)}e^{i(\rho x^2+2qx+r)}dx = \frac{\sqrt{\pi}}{\sqrt[4]{a^2+p^2}}\exp\left(\frac{a(b^2-ac)-(aq^2-2bq+cp^2)}{a^2+p^2}\right) \times\exp\left\{i\left[\frac{1}{2}\arctan\left(\frac{\rho}{a}\right) -\frac{p(q^2-pr)-(b^2p-2abq+a^2r)}{a^2+p^2}\right]\right\} \tag{44}$$

and the fully three-dimensional x-ray spectral brightness is now obtained as a function of the electron initial position and velocity, $\mathbf{x}_0$ and $\mathbf{u}_0$, as well as the laser parameters, and the scattered 4-wave-number, $k_\mu^s=(\omega_s,\omega_s\hat{\mathbf{n}})$. Frequencies are normalized to the laser pulse central wavelength, $k_0=\omega_0=1$, and axial positions are measured from the laser focal plane, lying at $z=0$. The complete result is quite complex, and was tracked analytically using MATHEMATICA [55].

A. The cold three-dimensional spectral density

Writing the cold (single electron) three-dimensional brightness as

$$\frac{\alpha A_0^2 \Delta\phi^2 w_{0x}^2 w_{0y}^2}{(4\pi)^2} S_0(k_\mu^s, x_\mu^0, u_\mu^0) = \frac{d^2 N_x}{d\omega\, d\Omega} = \frac{\alpha}{(4\pi)^3}\frac{\omega}{\kappa^2} A_0^2 w_{0x}^2 w_{0y}^2 \Delta t^2 \left| \hat{\mathbf{n}} \int\int_{\mathbb{R}^2} (\boldsymbol{\alpha} k_x^2 + \boldsymbol{\beta} k_y^2 + \boldsymbol{\gamma} k_x k_y + \boldsymbol{\delta} k_x + \boldsymbol{\varepsilon} k_y + \boldsymbol{\zeta}) \right.$$
$$\left. \times \exp[-(a k_x^2 + b k_y^2 + c k_x k_y + d k_x + e k_y + f)] \exp[i(p k_x^2 + q k_y^2 + r k_x + s k_y + t)] dk_x dk_y \right|^2 \tag{45}$$

we can introduce the following coefficients for the exponentials:

$$a = \frac{1}{4}\left\{ \frac{\Delta t^2 [u_x^2 - u_z(\kappa_a - \kappa)]}{\kappa^2} + w_{0x}^2 \right\},$$
$$b = \frac{1}{4}\left\{ \frac{\Delta t^2 [u_y^2 - u_z(\kappa_a - \kappa)]}{\kappa^2} = w_{0y}^2 \right\},$$
$$c = \frac{\Delta t^2 u_x u_y}{2\kappa^2}, \quad d = \frac{\Delta t^2 u_x(\kappa_s - \kappa)}{2\kappa^2},$$
$$e = \frac{\Delta t^2 u_y(\kappa_s - \kappa)}{2\kappa^2}, \quad f = \frac{\Delta t^2 (\kappa_s - \kappa)^2}{4\kappa^2}, \tag{46}$$
$$p = -\frac{\gamma z_0}{2\kappa}, \quad q = -\frac{\gamma z_0}{2\kappa}, \quad r = x_0 + \frac{u_x z_0}{\kappa},$$
$$s = y_0 + \frac{u_y z_0}{\kappa}, \quad t = \frac{\kappa_z z_0}{\kappa};$$

furthermore, the curl operator, expressed in transverse momentum space, yields the following vector components:

$$\alpha_x = \frac{\gamma\kappa_s - 2u_x^2 + 2\kappa u_z}{2\kappa\kappa_s}, \quad \alpha_y = 0,$$
$$\alpha_z = \frac{\kappa u_x u_z - u_x^3 + u_x \gamma \kappa_s}{\kappa^2 \kappa_s},$$
$$\beta_x = \frac{\gamma}{2\kappa}, \quad \beta_y = -\frac{u_x u_y}{\kappa\kappa_s}, \quad \beta_z = \frac{-u_x u_y^2 + u_x \gamma \kappa_s}{\kappa^2 \kappa_s},$$
$$\gamma_x = -\frac{u_x u_y}{\kappa\kappa_s}, \quad \gamma_y = \frac{\kappa u_z - u_x^2}{\kappa\kappa_s}, \quad \gamma_z = \frac{\kappa u_y u_z - 2u_x^2 u_y}{\kappa^2 \kappa_s}, \tag{47}$$
$$\delta_x = -2\frac{u_x}{\kappa}, \quad \delta_y = 0, \quad \delta_z = 1 + \frac{u_z}{\kappa} - 2\frac{u_x^2}{\kappa^2},$$
$$\varepsilon_x = -\frac{u_y}{\kappa}, \quad \varepsilon_y = -\frac{u_x}{\kappa}, \quad \varepsilon_z = -2\frac{u_x}{\kappa}\frac{u_y}{\kappa},$$
$$\zeta_x = -\frac{\kappa_s}{\kappa}, \quad \zeta_y = 0, \quad \zeta_z = -\frac{\kappa_s u_x}{\kappa^2}.$$

These terms are functions of the laser parameters, as well as the scattering 4-wave-number k_μ^s, and the electron initial position x_μ^0 and velocity u_μ^0; therefore the 6-dimensional electron phase space now appears explicitly in the three-dimensional spectral density of the scattered x rays. Finally, the incident and scattered light-cone variables are

$$\kappa = \gamma - z_z, \quad \kappa_s = \omega(\gamma - \hat{\mathbf{n}}\cdot\mathbf{u}). \tag{48}$$

The advantage of a fully analytical treatment of the problem, afforded by the use of the paraxial propagator formalism, resides in the much shorter computing time required to map the radiation produced by each electron in the beam.

A much simplified form of the general result is obtained by considering a centered electron, where $\mathbf{x}_0 = \mathbf{0}$: in this case,

$$\frac{d^2 N(k_\mu^s)}{d\omega_s d\Omega} = \frac{\alpha\omega_s A_0^2}{4\pi\kappa_0^2}\eta_x \eta_y \eta_t |\hat{\mathbf{n}}\times\mathbf{v}(u_\nu^0, x_\nu^0 k_\mu^s)|^2 \times \exp\left\{ -\frac{\Delta\phi^2(\chi-1)^2 + \mathcal{F}(u_\nu^0, x_\nu^0, k_\mu^s)}{2\left[1 + \eta_x \Delta\phi^2 \left(\frac{u_x}{\overline{w}_x}\right)^2 + \eta_y \Delta\phi^2 \left(\frac{u_y}{\overline{w}_y}\right)^2\right]} \right\}. \tag{49}$$

Here, we have defined $\overline{w}_{x,y} = \kappa_0 w_{0,x,y}$, and the normalization constants

$$\eta_{x,y}(k_\mu^s) = \frac{\overline{w}_{x,y}^2}{\overline{w}_{x,y}^2 + \Delta\phi^2 u_z(\kappa_0 - \kappa_s)},$$
$$\eta_t(k_\mu^s) = \left[\Delta\phi^{-2} + \eta_x\left(\frac{u_x}{\overline{w}_x}\right)^2 + \eta\left(\frac{u_y}{\overline{w}_y}\right)^2\right]^{-1}; \tag{50}$$

we have also introduced the normalized Doppler-shifted frequency $\chi(u_\nu^0, k_\mu^s) = \kappa_s/\kappa_0$. Equation (50) indicates that the minimum x-ray spectral width is given by the laser pulse duration; it also shows that three-dimensional effects change the x-ray spectrum because of the convective terms due to the electron crossing the laser focus. The vector $\mathbf{v}(u_\nu^0, x_\nu^0, k_\mu^s)$, and the function $\mathcal{F}(u_\nu^0, x_\nu^0, k_\mu^s)$ both depend on the initial position of the electron; when $x_\nu^0 = \emptyset$, $\mathcal{F} = 0$. In addition, in the specific cases of transverse or axial collisions, $|\hat{\mathbf{n}}\times\mathbf{v}|^2$ takes a relatively simpler form:

$$|\hat{\mathbf{n}}\times\mathbf{v}(\hat{\mathbf{z}}u_z,\emptyset,k_\mu^s)|^2=|\hat{\mathbf{n}}\times\hat{\mathbf{x}}|^2\left[\frac{\eta_x\kappa_0(2\kappa_0u_z+\gamma\kappa_s)}{\overline{w}_x^2\kappa_s}+\frac{\eta_y\kappa_0\gamma}{\overline{w}_y^2}-\frac{\kappa_s}{\kappa_0}\right]^2, \tag{51}$$

$$\frac{|\hat{\mathbf{n}}\times\mathbf{v}(\hat{\mathbf{y}}u_y,\emptyset,k_\mu^s)|^2}{|\hat{\mathbf{n}}\times\hat{\mathbf{x}}|^2}=\left\{\frac{\kappa_0\gamma}{\overline{w}_x^2}-\frac{\kappa_s}{\kappa_0}-\frac{\Delta\phi^2u_y^2(\kappa_0-\kappa_a)-\dfrac{\gamma\kappa_0^2u_y^2}{\Delta\phi^2u_y^2+\overline{w}_y^2}\left[\Delta\phi^2+\dfrac{\Delta\phi^4}{2}\left(1-\dfrac{\kappa_s}{\kappa_0}\right)^2+\dfrac{\overline{w}_y^2}{u_y^2}\right]}{\kappa_0(\Delta\phi^2u_y^2+\overline{w}_y^2)}\right\}^2, \tag{52}$$

$$\frac{|\hat{\mathbf{x}}\times\mathbf{v}[\hat{\mathbf{x}}u_x,\emptyset,\omega_s(1,\hat{\mathbf{x}})]|^2}{|\hat{\mathbf{x}}\times\hat{\mathbf{z}}|^2}=\left\{\frac{\kappa_0\gamma}{\hat{w}_y^2}-\frac{\kappa_s}{\kappa_0}-\frac{2\Delta\phi^2u_x^2(\kappa_0-\kappa_s)+\dfrac{\gamma\kappa_s-2u_x^2}{2\kappa_s}[\Delta\phi^4u_x^2(\kappa_0-\kappa_s)^2+2\kappa_0^2(\Delta\phi^2u_x^2+\overline{w}_x^2)]}{\kappa_0(\Delta\phi^2u_x^2+\overline{w}_x^2)}\right\}^2. \tag{53}$$

B. Three-dimensional effects

The physics underlying these results can be summarized as follows: first, the one-dimensional kernel $(\alpha\omega_sA_0^2\Delta\phi^2/4\pi\kappa_0^2)\exp\{-(\Delta\phi^2/2)[\chi(\omega,\gamma,\theta,\varphi)-1]^2\}$ always appears, indicating that the scattered radiation spectrum peaks near the Doppler-shifted frequency $\chi=1$; furthermore, the scattering is proportional to the laser pulse energy $A_0^2\Delta\phi$, and the minimum spectral width is given by that of the laser, $\Delta\phi^{-1}$; second, the interaction geometry modifies the spectral width, as illustrated in Fig. 6; in the case of a transverse interaction, wider bandwidths can be obtained for narrow focal spots, corresponding to the aforementioned shorter effective interaction time due to the convective motion of the electron through the focus; in addition, the spread of incidence angle $\Delta\varphi\simeq\pi\lambda_0/w_0$, corresponding to smaller spot sizes plays an important role when $\varphi_0=\pi/2$, because of the $\cos\varphi_0$ behavior of the differential scattering cross section; by contrast, when $\varphi_0=\pi$, these corrections are quadratic and nearly negligible; third, in the case where the initial velocity is in the direction of polarization, shown in Fig. 6, the radiation observed along that direction results from the axial component of the 4-potential, which is a purely three-dimensional effect; finally, we note that for larger values of the focal spot size, around $w_0=100\,\mu$m, the spectra converge to the minimum spectral width of the laser regardless of the interaction geometry.

A systematic study of three-dimensional effects, including timing jitter, electron beam and laser pulse spatial overlap, as well as varying interaction geometry, is given in Sec. V, where we present the three-dimensional code developed from the formalism derived here.

V. THREE-DIMENSIONAL COMPTON CODE

In order to fully exploit the results derived in Sec. IV, we have developed a three-dimensional code describing the radiation scattered by a distribution of N_e point charges having the same charge-to-mass ratio as electrons. The $6N_e$-dimensional phase space is generated by randomly loading the particles in prescribed statistical distribution, or can be the output of an electron beam optics code, such as PARMELA. The interface of PARMELA [56] to our three-dimensional code will be described in detail in an upcoming paper; here, we will focus on a $6N_e$-dimensional phase-space model using Gaussian distribution: a given particle, numbered $1\leqslant i\leqslant N_e$, is assigned a random position, $(\mathbf{x}_i^0,\mathbf{u}_i^0)$, in phase space; its charge is then scaled as

$$q_i=\exp\left[-\left(\frac{x_i^0-x_0}{\Delta x}\right)^2-\left(\frac{y_i^0-y_0}{\Delta y}\right)^2-\left(\frac{z_i^0-z_0}{\Delta z}\right)^2-\left(\frac{u_{xi}^0-u_{x0}}{\Delta u_x}\right)^2-\left(\frac{u_{yi}^0-u_{y0}}{\Delta u_y}\right)^2-\left(\frac{u_{zi}^0-u_{z0}}{\Delta u_z}\right)^2\right], \tag{54}$$

to reflect the probability distribution. Here, x_0 and y_0 now correspond to transverse spatial offsets, z_0 represents timing jitter, Δx and Δy are the electron bunch waist size, while Δz is the bunch duration; $\mathbf{u}_0$ corresponds to the electron beam incidence, while Δu_x and Δu_y are related to the beam horizontal and vertical emittance; finally, Δu_z represents energy spread. Note that far from head-on collisions, one needs to perform the appropriate projections to correctly relate the quantities discussed above to the conventional parameters describing the electron beam phase space; we also note that the random Gaussian loading technique presented here does not include correlations found in typical beams modeled by PARMELA; for our current purpose, however, this model proves entirely sufficient as it allows us to verify the accuracy of the one-dimensional theory of emittance and energy spread developed in Sec. III, and to benchmark the code in the plane wave limit; it also allows for the systematic study of the x-ray spectral brightness degradation under a variety of conditions closely approaching experimental constraints. The code keeps track of the total charge, $\Sigma_{i=1}^{N_e}q_i$, and after performing the incoherent summation over all particles, the charge is rescaled to the desired value.

The terms in Eqs. (46) and (47) are easily tracked by the code, and formula (44) is used twice to perform the integrals over the k_x and k_y components of the transverse wave number, as prescribed in Eq. (45). In running the code initially, it was determined that good statistical convergence is obtained for $N_e\geqslant3\times10^4$; generally, we have used 50 000 particles in the results presented here. Two different types of output data files are created by the code: spectral brightness measured at a prescribed scattering angle, or angular maps at a specified

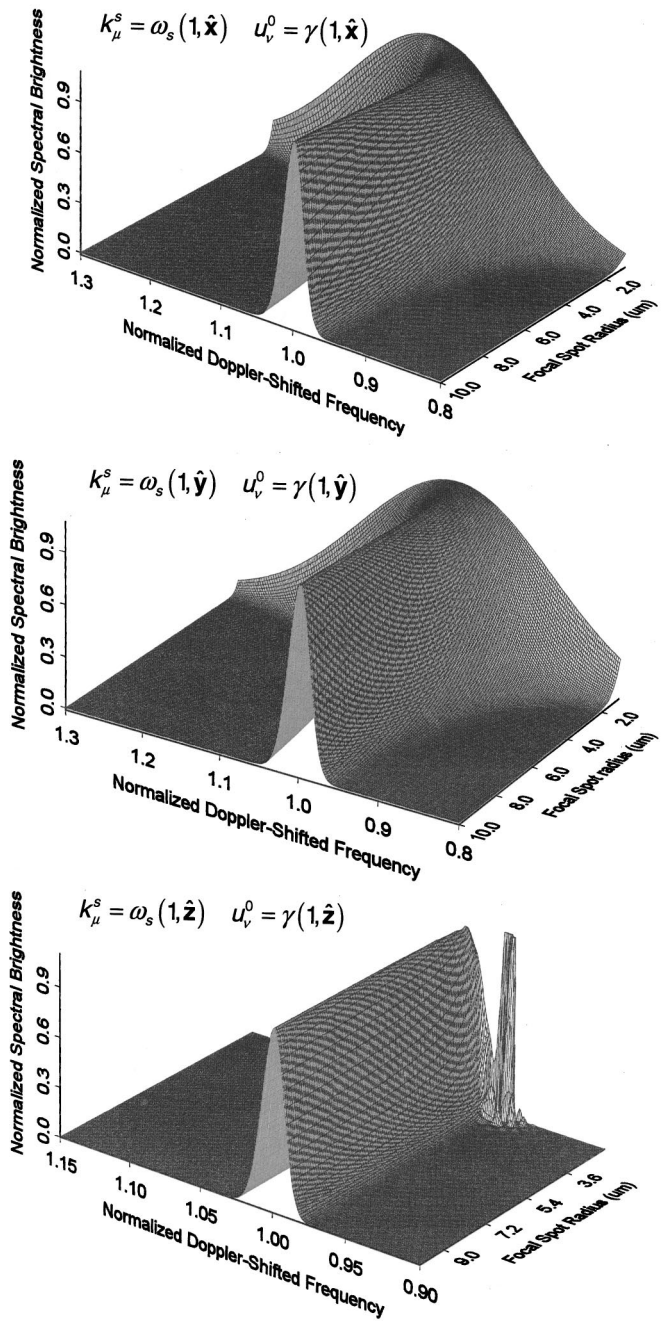

FIG. 6. On-axis spectral brightness as a function of the Doppler-shifted frequency and focal radius for transverse interactions; each spectrum is normalized to unity to clearly exhibit the broadening and frequency shift. Here, $\gamma=50$, $\lambda_0=800$ nm, and $\Delta t=50$ fs. The spurious peak on the bottom graph corresponds to a regime where the condition $\kappa_0^2 w_{0x,y}^2 > \Delta\phi^2[u_z(\kappa_s-\kappa_0)-u_{x,y}^2]$ is violated.

x-ray frequency; for angular maps, the code also integrates the flux over the map, in a small (typically 1 eV) x-ray photon energy interval. This last result is important for x-ray protein crystallography and other applications.

We have first systematically studied the effects of energy spread, emittance, electron beam focal spot size, bunch duration, and timing jitter. For the sake of clarity, we have chosen cylindrical foci: $\Delta x=\Delta y$ and $w_{0x}=w_{0y}$. To distinguish between the various effects, we have varied each time one of the parameters listed above, while maintaining all other parameters equal to zero, and the radiation frequency $\chi=1$; furthermore, to help comparing the various effects, we have normalized the brightness. The results are given in Fig. 7, and very clearly show that the various degradation mechanisms studied yield similar curves, roughly scaling as $1/\sqrt{1+\xi^2}$, where ξ represents the degradation parameter, properly scaled; for example, in the case of energy spread,

$$\xi=\frac{\Delta\phi}{\sqrt{2}}\frac{\Delta\gamma}{\gamma_0}\frac{\omega}{\gamma_0^2}\frac{\cos\varphi-\cos\theta}{(1-\cos\varphi)^2}.$$

From an experimental point of view, the most stringent requirements are clearly on emittance and energy spread. Finally, the optimum electron beam size does not correspond to a match with the laser mode; rather, the beam should be focused as tightly as possible within the laser focal spot. This can easily be understood, if we consider the laser pulse as an electromagnetic wiggler, which has maximal field strength, or photon density, on-axis. For high-energy beams, where emittance and space-charge effects are very small, and can therefore be focused over a few tens of nm, this is a potentially important result. We also note that this conclusion does not hold if the laser beam depletion becomes important.

The case of a realistic beam is presented in Figs. 8 and 9. The laser parameters are as follows: $\lambda_0=800$ nm, $w_0=10\,\mu$m, $\Delta t=200$ fs, and a pulse energy of 50 mJ. The electron bunch energy is 22.75 MeV, its charge is 0.5 nC, the relative energy spread is $\Delta\gamma/\gamma_0=0.5\%$, the beam normalized emittance is 1π mm×mrad, and the focal spot size matches the laser focal distribution. A repetition rate of 1 kHz is used to scale the average spectral brightness of the source; the maximum brightness compares well with that produced by bend magnets on synchrotron beamlines. The angle of incidence is 180°, and the spectra are observed on-axis; the angular maps are obtained at the spectral maximum. One-dimensional, cold beam results are shown for comparison in Fig. 3, and clearly demonstrate the importance of the theoretical model developed here, as the warm, three-dimensional brightness is seen to be considerably smaller than that predicted by a simple one-dimensional theory.

We also note that the laser-driven Compton source can produce much shorter x-ray flashes than those currently generated at synchrotrons: sub-100-fs pulses will be readily produced, in contrast with FWHM in the 35–100-ps range at the Advanced Light Source and 170 ps at the Advanced Photon Source (APS) [29].

VI. X-RAY PROTEIN CRYSTALLOGRAPHY

One important application identified and targeted for the 0.9-Å Compton x-ray source is protein crystallography; in this section, a broad outline is given, while for details, we refer the reader to Sec. 5 of the Appendix. Recombinant DNA technology [33] is used to produce large quantities of a given protein by introducing the corresponding coding DNA sequence into the genetic material of a bacterium. Overexpression of large quantities of the protein is induced, and the

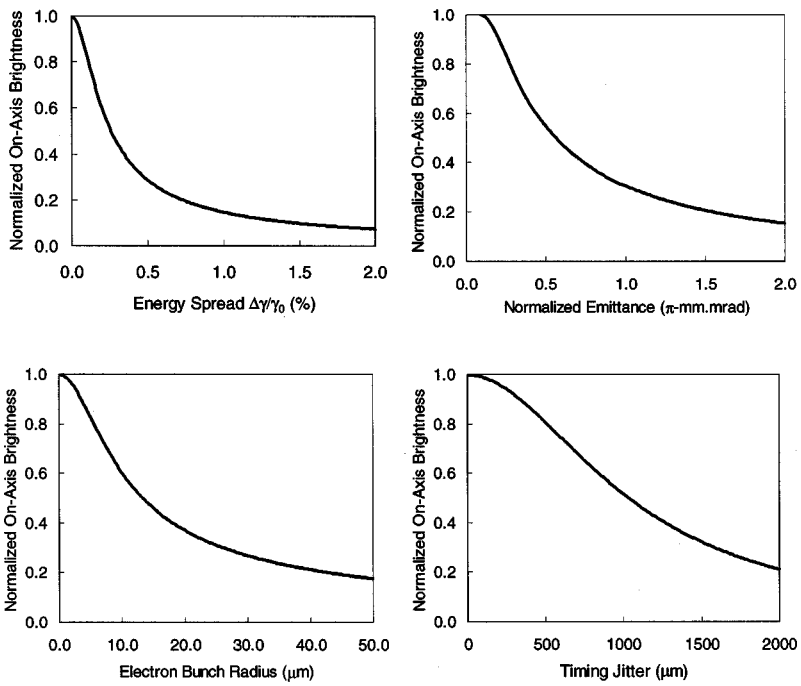

FIG. 7. Degradation of the on-axis x-ray spectral brightness as a function of energy spread (top left), emittance (top right), electron bunch radial beam overlap (bottom left), and timing jitter (bottom right); the other parameters are maintained equal to zero and the beam energy is 22.75 MeV, the bunch charge is 0.5 nC, its duration is 1 ps; the laser wavelength is $\lambda_0 = 800$ nm, $w_0 = 10\ \mu$m, and the laser pulse energy is 50 mJ.

protein is extracted and purified. Single crystals of the protein are grown in solution, and diffraction data (intensities of lattice reflections) are collected at cryogenic temperatures to minimize radiation damage. To reconstruct the three-dimensional electron density of the molecule by Fourier methods, two terms per reflection are needed: the structure factor amplitudes, which are readily measured as the square root of the reflection intensities, and the phase angle for each reflection, which is not directly obtainable from protein data (the ''phase problem'' in crystallography). The most powerful method to solve the phase problem is MAD phasing, where experimental phase information is obtained from dispersive differences between, and anomalous (Bijvoet) differences within, data sets collected at different wavelengths around the absorption edge of anomalously scattering atoms introduced in the protein [27,28,38]. (See Fig. 10.)

This approach, first demonstrated at dedicated synchrotron beamlines, has proven extremely successful, for example, to provide the structural information crucial for the *ab initio* design of inhibitor molecules targeting specific binding sites on proteins such as the HIV protease, thus providing a paradigm for systematic drug design and development [34]. As synchrotrons are large and expensive facilities,

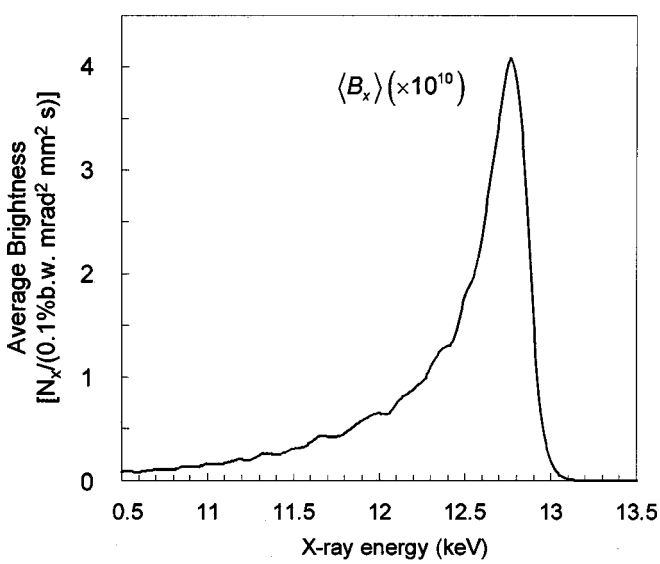

FIG. 8. On-axis, average x-ray spectral brightness backscattered by a 22.75-MeV, 0.5-nC, 1-ps electron bunch; $\lambda_0 = 800$ nm, 50 mJ, $w_0 = r_b = 10\ \mu$m cylindrical focus, $\varphi_0 = 180°$, $A_0 = 0.17$; the repetition rate is 1 kHz.

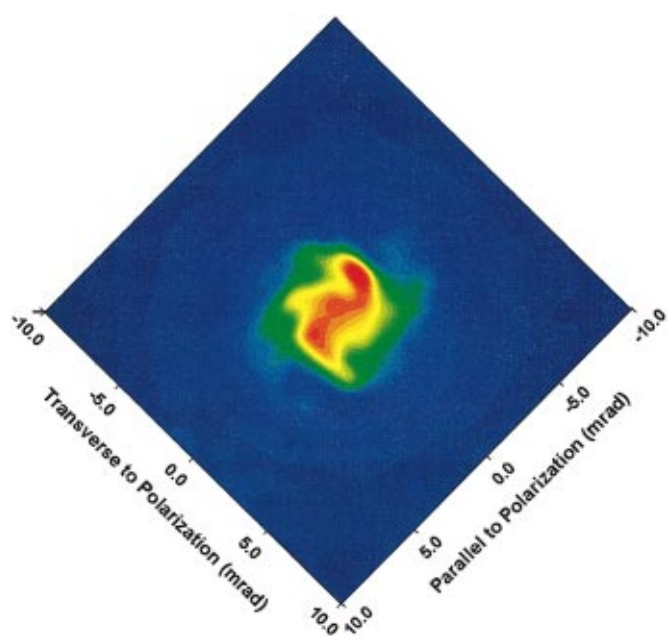

FIG. 9. (Color) Angular map of the x-ray spectral brightness; the other parameters are as in Fig. 8, and the x-ray energy is 12.66 keV.

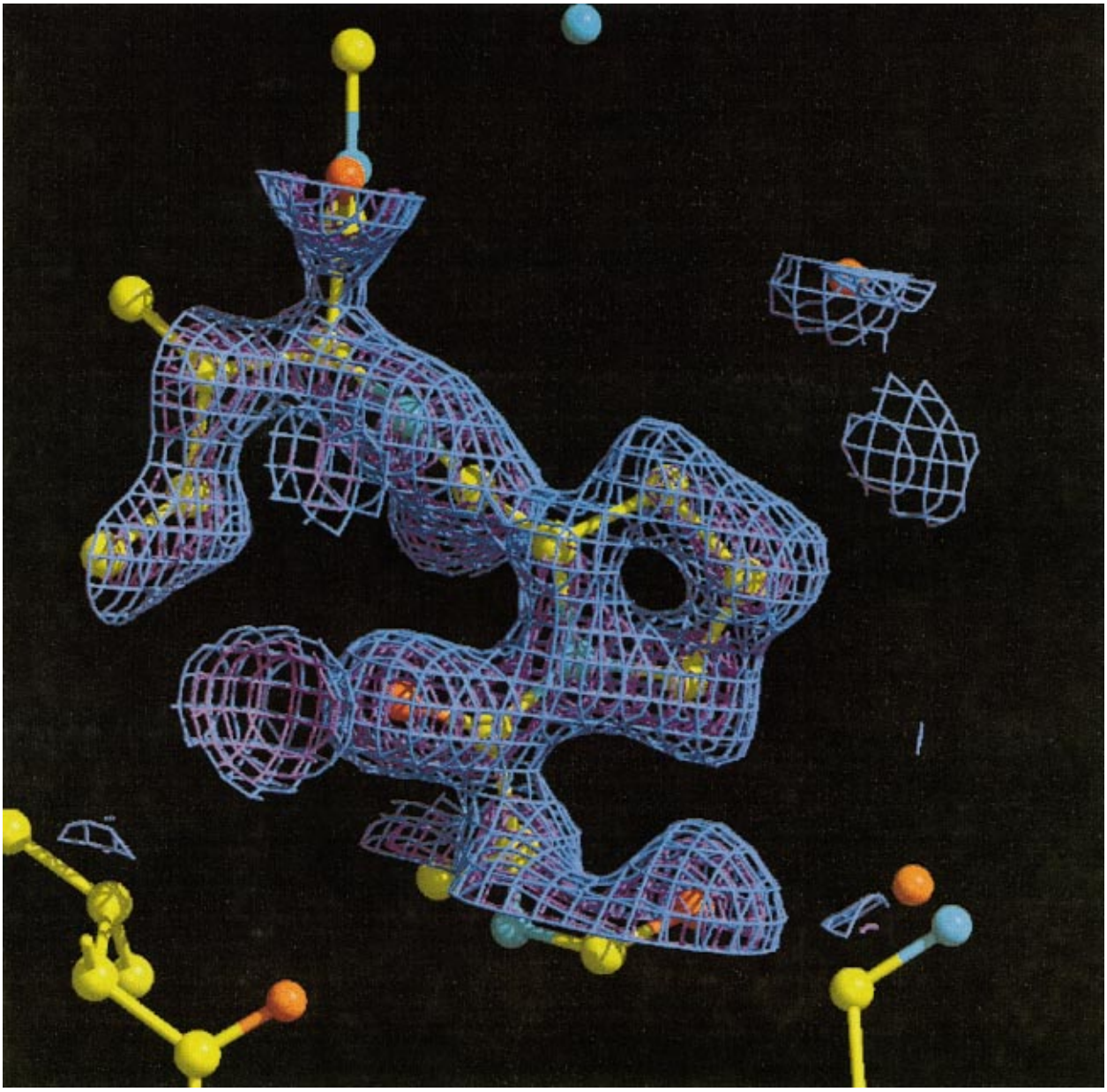

FIG. 10. (Color) Section of electron density map and protein structure model. After initial protein phases are obtained, a model of the protein (ball-and-stick model, yellow: carbon atoms; blue: nitrogen atoms, red: oxygen atoms and water molecules) is built into the solvent-flattened electron density map (blue three-dimensional grid) using real space fitting. The selected region is a three-residue stretch out of the 233 residues comprising the structure of a rationally designed, engineered Staphylococcal enterotoxin A (SEA) mutant vaccine [62]. The hole in the proline ring indicates that displayed electron density map is of high quality (1.5 Å resolution).

our goal is to develop compact, tunable, x-ray sources with nearly comparable characteristics at a fraction of the cost. Laser-driven Compton scattering allows one to use a much lower electron beam energy (tens of MeV instead of GeV), while retaining the tunability distinguishing synchrotrons from conventional x-ray sources. The combination of a tabletop, terawatt-class laser with an integrated, high-brightness, relativistic photoelectron source will result in such a compact x-ray source, provided that the combined quality of the electron and laser beams is sufficiently high.

In recent years, molecular biology has yielded tremendous advances in our understanding of the basic mechanisms underlying the biology of multicellular organisms, as exemplified by the Human Genome Project (HGP) [30] and the emergence of recombinant DNA technology [33]. These advances have resulted in novel approaches to the systematic diagnosis and treatment of a broad range of illnesses: for example, a detailed understanding of the expression of proto-oncogenes might lead to highly efficient new strategies to fight cancer. With the HGP nearing full completion, the attention of the biomedical research community is rapidly shifting to the fundamental problem of protein structure and function, or structural genomics [31,32].

Within this context, x-ray protein crystallography is one

of the foremost tools to study the three-dimensional structure of proteins. As recently demonstrated by the development of HIV protease inhibitors [35,36], x-ray protein crystallography is a key enabling technology for rational drug design and development [34].

A. Multiwavelength anomalous diffraction

One of the key challenges in protein crystallography is the determination of the phase of the diffracted waves, which is determined by the absolute spatial position of each diffracting atom in the lattice [57]. The electron density in the crystallized protein is obtained by performing the Fourier summation:

$$\rho(x,y,z)=\frac{1}{V}\sum_{h=-\infty}^{+\infty}\sum_{k=-\infty}^{+\infty}\sum_{l=-\infty}^{+\infty}|F(h,k,l)| \times\exp\{-2\pi i[hx+ky+lz-\varphi(h,k,l)]\}, \tag{55}$$

where $|F(h,k,l)|$ is the structure factor amplitude of reflection (h,k,l), including the temperature factor, and $\varphi(h,k,l)$ is the phase angle to be determined. The x-ray detector measures the diffracted intensity, $I(h,k,l)\propto|F(h,k,l)|^2$; therefore, additional information is required to determine the phase in order to perform the three-dimensional Fourier summation in Eq. (55).

In the case where a crystal contains anomalous scatterers (either as heavy atoms soaked into the protein crystals or introduced into the protein as Se-methionine) [58], one can exploit the differences in intensity between Bijvoet pairs within a data set, and dispersive differences between data sets recorded at different wavelengths, to determine the reflection phase angles [59–61]. In MAD, the strong wavelength dependence of the anomalous scattering around an x-ray absorption edge is used: typical spectral widths for well-defined K or L edges are of the order of a few eV. The wavelengths must be correspondingly carefully chosen to optimize the anomalous and dispersive signal (see Fig. 11). Many high-Z elements, which can be incorporated into proteins, give rise to sufficiently strong anomalous signals. Hendrickson showed that the presence of a single Se atom in a protein of up to approximately 150 amino acid residues is sufficient to determine phases via MAD [58]. A single heavy atom like Au or Hg can have the power to phase 300 or more residues. Several anomalous scatterers present in a single crystal allow the phase determination of correspondingly larger structures.

B. Protein data acquisition time

We now compare the calculated radiation characteristics of the Compton source with the two main sources currently used for x-ray protein crystallography: rotating anode x-ray sources and synchrotrons. As one must match the x-ray beam divergence to the crystal mosaicity for high-resolution data collection, the 3.5-mrad half-angle of the x-ray cone produced in our simulations is a very encouraging result, as it matches the mosaicity of the best protein crystals, $>0.2°$.

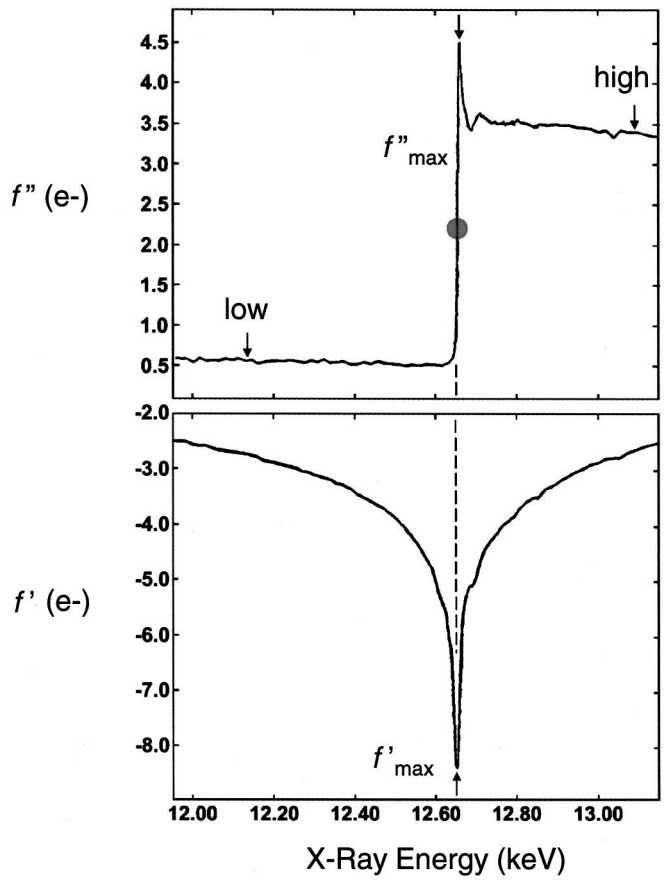

FIG. 11. Selection of wavelengths for a MAD experiment. Actual normalized absorption edge scan of Se in a Se-Methionine labeled protein [63]. The atomic scattering factor f contains a significant wavelength dependent contribution at the absorption edge: $f=f_0+f'+if''$. The top part represents the imaginary component of the anomalous, wavelength dependent scattering factor f'', while the lower graph shows the real part f', obtained from the measured absorption signal, using the Kramers-Kronig transformation. Note that the magnitude of f' and f'' is only a few electrons. Careful selection of the wavelengths is thus necessary to optimize the MAD data collection. At the peak of the absorption edge (f''_{MAD}), the anomalous signal difference between Bijvoet (or Friedel) pairs within a data set is maximized. The largest dispersive difference between data sets recorded at different wavelengths can be achieved against data collected at the minimum of the real part of the anomalous scattering factor (f'). The arrows labeled high and low represent the remote wavelengths used in the creation of additional dispersive differences. From a number of differences a combined, best anoamolous difference data set is created, from which, in turn, the heavy atom positions, needed in the phasing process, can be determined by Patterson and/or direct methods [64].

A simple comparison can be made by considering the average spectral brightness of different sources; the results are typically given in units of photons per 0.1% bandwidth, per mm^2, per mrad^2, s) [29]. For modern rotating anode sources, given a 2.6-eV width for the $K_{\alpha 1}$ line of copper at 1.540 51 Å and up to 98% flux in that line, an average brightness around 10^9 is possible; synchrotron bending magnets reach 10^{15} at 10 keV for a 6–8-GeV ring, while a 72-period, 3.3-cm wavelength undulator produces 9.4-keV photons with

a brightness of 4.8×10^{18} at the APS [29]; however, brightnesses $>10^{12}$ begin to cause severe radiation damage. The Compton source generates 12.77-keV photons with a brightness of 4.1×10^{10}; this compares quite favorably with rotating anode x-ray sources, especially in view of added tunability, which is indispensable for MAD. A more detailed comparison is given in Sec. 5 of the Appendix.

C. The micro-MAD concept

A unique characteristic of the Compton source is the very small size of the x-ray source, which essentially matches that of the laser focal spot size; for imaging applications, this translates into increased contrast and better resolution. This also has important implications for microcrystals, which are more easily produced and often are of better quality (i.e., diffracting to higher resolution with smaller mosaicity) than larger ones. Cooling also becomes less problematic in smaller crystals due to the lower amount of heat generated and the more advantageous surface-to-volume ratios. Therefore, the Compton x-ray source seems almost ideally suited for the development of a compact, user-friendly, tunable x-ray source, with an average brightness comparing well with that of rotating anode sources, and the capability of using MAD on microcrystals; this is the idea underlying the micro-MAD (μMAD) concept currently being evaluated at Lawrence Livermore National Laboratory.

VII. CONCLUSIONS

In this paper, we have given a detailed and extensive presentation of the three-dimensional theory of Compton scattering, where the influence of the electron beam phase-space topology, including the effects of emittance and energy spread, upon the scattered x-ray brightness is fully taken into account. The centerpiece of our theoretical model is embodied by the radiation theorem derived in Sec. II, which yields the three-dimensional spectral density scattered by a single charged particle in an arbitrary electromagnetic field distribution *in vacuo*, provided that the corresponding vector potential satisfies the condition $|eA/m_0c|^2\ll1$. We then apply this formalism to the case of a laser focus, and use the paraxial ray approximation to obtain a fully analytical solution; finally, incoherent summations are performed in the case of a distribution of charges. We have developed a three-dimensional Compton scattering code based on this formalism; the initial electron phase-space distribution can be modeled either using a random Gaussian loading scheme, which is useful to benchmark the code, and to compare the three-dimensional results with the analytical theory of emittance and energy spread derived in the one-dimensional limit and discussed in Sec. III, or by interfacing our code with an electron beam design code, such as PARMELA; in that case, the macroparticles pushed by PARMELA are propagated through the three-dimensional laser focus, and the radiation scattered by each charge is summed incoherently to obtain the corresponding x-ray brightness. Finally, a design example is discussed, and its relevance to x-ray protein crystallography is examined in detail; within this context, we introduce the μMAD concept, where we believe that the Compton source could be used to apply MAD to protein microcrystals with great benefits.

ACKNOWLEDGMENTS

This work was performed under the auspices of the U.S. Department of Energy by University of California Lawrence Livermore National Laboratory, through the Institute for Laser Science and Applications, under Contract No. W-7405-ENG-48, and was partially supported by NIH Contract No. N01-CO-97113 and AFOSR MURI Grant No. F49620-99-1-0297. One of us (F.V.H.) also acknowledges very stimulating discussions with D.T. Santa Maria and inspiring comments from L. Montagnier [36].

APPENDIX: COHERENCE, HARMONICS, AND RADIATIVE CORRECTIONS

This Appendix is mainly intended as a brief review, included here for the sake of completeness; however, the stochastic electron gas model is highly relevant to our analysis, as it justifies *a posteriori* the incoherent summation technique used to model the electron beam phase-space topology.

1. Stochastic electron gas model

To study the coherence of the radiation produced by an ensemble of electrons subjected to the drive laser field, a simple plane-wave model suffices: the electron 4-velocity is described by

$$\mathbf{u}_\perp(\tau)=\mathbf{A}_\perp(\phi),\quad u_z(\tau)=u_0+\frac{\kappa_0^{-1}}{2}\mathbf{A}_\perp^2(\phi),$$

$$\gamma(\tau)=\gamma_0\frac{\kappa_0^{-1}}{2}\mathbf{A}_\perp^2(\phi). \tag{A1}$$

Here, $u_0=\gamma_0\beta_0$ is the initial electron momentum. The 4-position of the interacting electron is then

$$x_\mu(\phi)=x_\mu(\phi=0)+\int_0^\phi\frac{dx_\mu}{d\tau}\frac{d\tau}{d\phi}d\psi$$

$$=x_{\mu0}+\kappa_0^{-1}\int_0^\phi u_\mu(\psi)d\psi. \tag{A2}$$

For a number of independent electrons, provided that space-charge effects can be neglected, the dynamics are identical, except for the fact that the initial positions vary. Again, as discussed by Jackson [51], the distribution of photons radiated per unit solid angle, per unit frequency is

$$\frac{d^2N_x(\omega,\hat{\mathbf{n}})}{d\omega\,d\Omega}=\frac{\alpha}{4\pi^2}\frac{\omega}{\kappa_0^2}\left|\sum_{n=1}^{N_e}\int_{-\infty}^{+\infty}\hat{\mathbf{n}}\times[\hat{\mathbf{n}}\times\mathbf{u}_n(\phi)]\times\exp\{i\omega[\phi+z_n(\phi)-\hat{\mathbf{n}}\cdot\mathbf{x}_n(\phi)]\}d\phi\right|^2, \tag{A3}$$

where N_x is the photon number, $\hat{\mathbf{n}}$ is the unit vector in the direction of observation, α is the fine-structure constant, N_e is the electron number, and where we have used the phase as the independent variable, as well as the invariance of $\kappa = \kappa_0$. As discussed above, $\mathbf{u}_n(\phi)$ can be replaced by the single-electron result obtained in Eq. (A1).

In the case of Compton backscattered radiation ($\hat{\mathbf{n}} = -\hat{z}$), Eq. (A3) reduces to

$$\frac{d^2N_x(\omega_1-\hat{z})}{d\omega\, d\Omega} = \frac{\alpha}{4\pi^2}\frac{\omega}{\kappa_0^2}\left|\sum_{n=1}^{N_e}\int_{-\infty}^{+\infty}\mathbf{A}_\perp(\phi) \times \exp\{i\omega[\phi+2z_n(\phi)]\}d\phi\right|^2; \quad \text{(A4)}$$

the axial position of each radiating electron must now be specified:

$$z_n(\phi) = z_n + \frac{u_0}{\kappa_0}\phi + \frac{1}{2\kappa_0^2}\int_0^\phi \mathbf{A}_\perp^2(\psi)d\psi, \quad \text{(A5)}$$

where z_n is the initial position of the nth electron. $\int_0^\phi \mathbf{A}_\perp^2(\psi)d\psi$ represents the relativistic mass correction of the ''dressed'' electron within the high-intensity laser pulse. The integral over phase and the sum over electrons are now separated:

$$\frac{d^2N_x(\omega_1-\hat{z})}{d\omega\, d\Omega} = \frac{\alpha}{4\pi^2}\chi\left|\int_{-\infty}^{+\infty}\mathbf{A}_\perp(\phi) \times \exp\left\{i\chi\left[\phi+\int_0^\phi \mathbf{A}_\perp^2(\psi)d\psi\right]\right\}\right|^2 \times \left|\sum_{n=1}^{N_e}\exp(i2\omega z_n)\right|^2. \quad \text{(A6)}$$

Here, $\chi = \omega[(1+\beta_0)/(1-\beta_0)]$ is the normalized Doppler-shifted frequency and $|\Sigma_{n=1}^{N_e}\exp(i2\omega z_n)|^2$ is the coherence factor [42,43].

In the case of a uniform initial electron distribution with random phase, illustrated in Fig. 12 (top), the coherence factor is simply the amplitude of a sum of phasors, each with unit length and a random angle. To show that the average length of the sum is given by $\sqrt{N_e}$, one can simply use a proof by recurrence: let us first assume that the average length of the first n phasors is $\sqrt{n}$; we now add a vector of unit length with random orientation, as shown in Fig. 12 (middle), and the new vector has a length given by $\sqrt{(\sqrt{n}+\cos\theta)^2+\sin^2\theta} = \sqrt{n+1+2\sqrt{n}\cos\theta}$. To obtain the average length of the new vector, we perform the integral over the random angle θ:

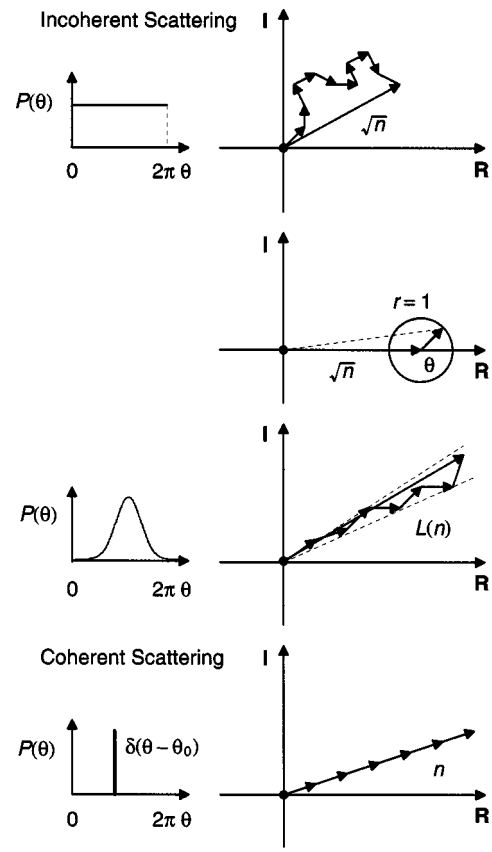

FIG. 12. Phasor summation and phase angle probability density for (from top to bottom) incoherent, partially coherent, and fully coherent scattering.

$$\langle\sqrt{|(\sqrt{n}+\cos\theta)\hat{x}+\hat{y}\sin\theta|^2}\rangle = \left[n+1+\frac{\sqrt{n}}{\pi}\int_0^{2\pi}\cos\theta\, d\theta\right]^{1/2} = \sqrt{n+1}, \quad \text{(A7)}$$

which proves the recurrence.

We have thus shown that $\langle|\Sigma_{n=1}^{N_e}\exp(i\theta_n)|^2\rangle = N_e$; this result is independent of the radiation frequency, because there are no boundary conditions to define a length scale. In a realistic situation, the initial electron distribution naturally defines a transition from coherent to incoherent radiation for a given wavelength: for electron distributions much shorter than that wavelength, the radiation process is expected to be coherent, while for longer bunches one should obtain incoherent radiation.

To properly model this situation, the derivation presented above must be modified: the key point in the derivation is to replace the average over the random phase angle performed in Eq. (A7) by a weighted average including the probability density of the initial phase. As derived previously, the length $\mathcal{L}(n+1)$ of $n+1$ phasors is given by

$$\mathcal{L}^2(n+1) = [\mathcal{L}(n)+\cos\theta]^2+\sin^2\theta = \mathcal{L}^2(n)+1+2\mathcal{L}(n)\cos\theta; \quad \text{(A8)}$$

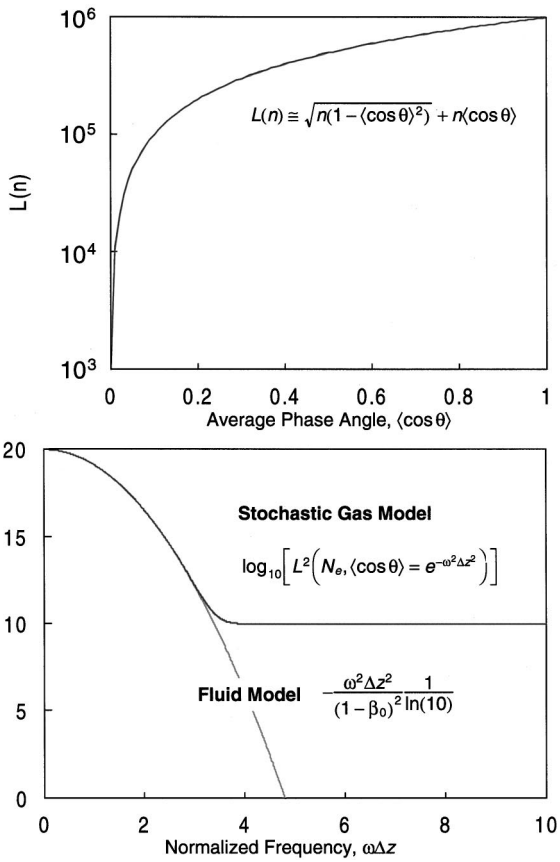

FIG. 13. Top: comparison between the average length on $n = 10^6$ phasors, as calculated exactly with a computer, and as derived from Eq. (A9). Bottom: logarithm of the effective number of radiating electrons as a function of the normalized bunch length, for both models.

averaging Eq. (A8) over the random phase angle, and taking the limit where $n \gg 1$, we find that

$$\mathcal{L}(n) = \sqrt{n(1-\langle\cos\theta\rangle^2)} + n\langle\cos\theta\rangle, \tag{A9}$$

with a relative error equal to $1/\sqrt{n}$. The accuracy of this solution is illustrated in Fig. 13 (top), where the behavior of $\mathcal{L}(n)$, calculated exactly with a computer, is shown as a function of $\langle\cos\theta\rangle$, and compared to Eq. (A9) for $n = 10^6$; the precision is excellent.

For incoherent radiation $\langle\cos\theta\rangle = 0$, and we recover the linear scaling of the radiated power with n; the case of coherent radiation corresponds to $\langle\cos\theta\rangle = 1$, for which the power scales as n^2. At this point, the averaging over the random phase angle must be specified; we have

$$\langle\cos\theta\rangle = \int_{-\infty}^{+\infty} P(\theta)\cos[\theta(z)]d\theta, \tag{A10}$$

where $P(\theta)$ is the probability density for the initial phase of the electron. $P(\theta)$ is directly related to the initial electron distribution by the relation $\theta = 2\omega z$, and is normalized: $\int_{-\infty}^{+\infty} P(\theta)d\theta = 1$. Here, a Gaussian bunch of width Δz is considered; the probability density takes the form

$$P[\theta(z)] = (1/\sqrt{\pi}2\omega\Delta z)\exp[-(z/\Delta z)^2],$$

and the average over the phase angle becomes

$$\langle\cos(\theta)\rangle = \eta(a) = \sqrt{a/\pi}\int_{-\infty}^{+\infty} e^{-a\theta^2}\cos\theta\, d\theta, \tag{A11}$$

where $a = 1/(2\omega z)^2$. The integral in Eq. (A11) can be performed analytically [53] to obtain

$$\langle\cos\theta\rangle = \exp(-\omega^2\Delta z^2) = e^{-1/2a}. \tag{A12}$$

In the case where the electron distribution is much longer than the radiation wavelength, $a \ll 1$, and $\eta(a) \to 0$; the coherence exponent approaches one half, and the radiation is incoherent. When the electron distribution is much shorter than the radiation wavelength, the probability density distribution approaches a Dirac delta function, with $\lim_{a\to\infty}(\sqrt{a/\pi}e^{-a\theta^2}) = \delta(\theta)$, and the radiated power scales as N_e^2. This is illustrated in Fig. 12: for incoherent scattering (top), each phasor angle has equal probability; $\langle\cos\theta\rangle = 0$, and the resulting superposition increases as $\sqrt{n}$. The case of fully coherent radiation is shown in Fig. 12 (bottom); here the angular probability density is a Dirac delta function, where $P(\theta) = \delta(\theta - \theta_0)$, the interference term, $\langle\cos\theta\rangle = 1$, and the phasor sum increases as n. Finally, an intermediate case is shown in Fig. 12 (middle); here the probability density indicates a preferred angular range, resulting in a superposition with an average length increasing as shown in Eq. (A9).

Thus, the power backscattered by an electron bunch is given by

$$\frac{d^2N_x(\omega,-\hat{z})}{d\omega\, d\Omega} = \frac{\alpha\chi}{4\pi^2}\mathcal{L}^2(N_e, \theta^{-\omega^2\Delta z^2})\left|\int_{-\infty}^{\infty}\mathbf{A}_\perp(\phi) \times\exp\left\{i\chi\left[\phi + \int_0^\phi \mathbf{A}_\perp^2(\psi)d\psi\right]\right\}d\phi\right|^2; \tag{A13}$$

as expected, the effective number of radiating electrons now depends explicitly on the wavelength and bunch size. For a linearly polarized Gaussian pulse, where $\mathbf{A}_\perp(\phi) = A_0\hat{x}e^{-i\phi-(\phi/\Delta\phi)^2}$, and with $A_0^2 \ll 1$, the Fourier transform yields

$$\frac{d^2N_x(\omega,-\hat{z})}{d\omega\, d\Omega} = \frac{\alpha}{16\pi}\chi A_0^2\Delta\phi^2\mathcal{L}^2(N_e, e^{-\omega^2\Delta z^2}) \times\exp\left[-\frac{(x-1)^2\Delta\phi^2}{2}\right]. \tag{A14}$$

2. Relativistic fluid model

To compare the stochastic electron gas to a relativistic fluid, we now consider the Lorentz force equation

$$\frac{du_\mu}{d\tau} = (u^\nu\partial_\nu)u_\mu = -(\partial_\mu A_\nu - \partial_\nu A_\mu)u^\nu, \tag{A15}$$

and the charge conservation, or continuity, equation $\partial_\mu j^\mu = 0$. Here, $u_\mu(x_\nu)$ is the 4-velocity field of the relativistic fluid, $A_\mu(x_\nu)$ is the 4-potential of the laser pulse, and the total derivative with respect to proper time is to be considered as a convective operator, as indicated. The 4-current density of the relativistic fluid is given by $j_\mu(x_\nu) = -n(x_\nu)u_\mu(x_\nu)/\gamma(x_\nu)$, where $n(x_\nu)$ is the density. Space-charge and radiation reaction [20,21,39,50] effects are neglected.

As the force equation is driven by the laser 4-potential that is a function of the fluid phase, $\phi(z,t)=t-z$, we seek a solution where the other fluid fields also depend on ϕ; the convective derivative operator reduces to

$$\begin{aligned}(u^\nu\partial_\nu)u_\mu(z,t) &= [\gamma\partial_t + u_z\partial_z]u_\mu(\phi)\\ &= \left(\gamma\frac{\partial\phi}{\partial t}+u_z\frac{\partial\phi}{\partial z}\right)\frac{du_\mu}{d\phi}\\ &= (\gamma-u_z)\frac{du_\mu}{d\phi}.\end{aligned} \tag{A16}$$

The Lorentz force equation now reads $(\gamma-u_z)d\mathbf{u}/d\phi = -(\gamma\mathbf{E}+\mathbf{u}\times\mathbf{B})$; in addition, energy conservation yields $(\gamma-u_z)d\gamma/d\phi = -\mathbf{u}\cdot\mathbf{E}$. The electromagnetic field components are given by $F_{\mu\nu}=\partial_\mu A_\nu - \partial_\nu A_\mu$. The evolution of the momentum field can be separated into a transverse and an axial component:

$$\begin{aligned}&(\gamma-u_z)\frac{d}{d\phi}(\mathbf{u}_\perp-\mathbf{A}_\perp)=\mathbf{0},\\ &(\gamma-u_z)\frac{du_z}{d\phi}=\mathbf{u}_\perp\cdot\frac{d\mathbf{A}_\perp}{d\phi}=(\gamma-u_z)\frac{d\gamma}{d\phi}.\end{aligned} \tag{A17}$$

We recover the transverse canonical momentum invariant, $\mathbf{u}_\perp-\mathbf{A}_\perp$; Eq. (A17) also shows that the light-cone variable is a fluid invariant. The sought-after fluid equilibrium is

$$u_z(z,t)=u_z(\phi)=u_{z0}+\kappa_0^{-1}\left[\mathbf{A}_\perp(\phi)\cdot\mathbf{u}_{\perp 0}+\frac{\mathbf{A}_\perp^2(\phi)}{2}\right], \tag{A18}$$

and

$$\gamma(z,t)=\gamma(\phi)=\gamma_0+\kappa_0^{-1}\left[\mathbf{A}_\perp(\phi)\cdot\mathbf{u}_{\perp 0}+\frac{\mathbf{A}_\perp^2(\phi)}{2}\right]. \tag{A19}$$

To determine the density, we seek a solution to the charge conservation equation where the density field is a function of the phase: the continuity equation reads

$$\begin{aligned}\partial_l n(\phi)+\nabla\cdot[n(\phi)\beta(\phi)] &= \frac{\partial\phi}{\partial t}\frac{dn}{d\phi}+\frac{\partial\phi}{\partial z}\frac{d}{d\phi}(n\beta_z)\\ &= \frac{d}{d\phi}[n(1-\beta_z)]\\ &= 0.\end{aligned} \tag{A20}$$

Multiplying and dividing the density by the energy, we can rewrite Eq. (A20) in terms of the light-cone variable,

$$\frac{d}{d\phi}\left[\frac{n}{\gamma}(\gamma-u_z)\right]=\frac{d}{d\phi}\left(\frac{n}{\gamma}\kappa\right)=\kappa_0\frac{d}{d\phi}\left(\frac{n}{\gamma}\right)=0; \tag{A21}$$

where $n(\phi)/\gamma(\phi)$ is a relativistic fluid invariant. This is an important result, as it shows that the relativistic plasma frequency is invariant: the density modulation induced by the laser radiation pressure exactly compensates the variation of the fluid energy within the pulse. We finally find

$$n(z,t)=n(\phi)=n_0\left\{1+\kappa_0^{-1}\left[\mathbf{A}_\perp(\phi)\cdot\mathbf{u}_{\perp 0}+\frac{\mathbf{A}_\perp^2(\phi)}{2}\right]\right\}, \tag{A22}$$

where n_0 is the initial electron beam density.

Having defined the fluid dynamical variables, we can derive the distribution of energy radiated by the fluid per unit solid angle, per unit frequency, by Fourier transforming the 4-current into momentum space [51]:

$$\begin{aligned}\frac{d^2N_z(\omega,\hat{\mathbf{n}})}{d\omega\, d\Omega} &= \frac{\alpha}{4\pi^2}\omega\left|\int_{\mathbb{R}^4}d^4x_\mu\hat{\mathbf{n}}\times[\hat{\mathbf{n}}\times\mathbf{j}(x_\mu)]\right.\\ &\quad\left.\times\exp[i\omega(t-\hat{\mathbf{n}}\cdot\mathbf{x})]\right|^2,\end{aligned} \tag{A23}$$

where $\mathbf{j}(x_\mu)$ is given by $\mathbf{j}=-n\beta=-n_0(\gamma/\gamma_0)\beta = -(n_0/\gamma_0)\mathbf{u}$.

The initial density distribution of the unmodulated beam has the form $n_0(x_\mu)=\rho f(\zeta)$, where we have defined the electron beam phase $\zeta(z,t)=z-\beta_0 t$, and where $f(\zeta)$ is the normalized axial envelope of the bunch, which propagates with the axial velocity β_0; the normalization constant ρ is defined by the total charge in the bunch: $\rho\int_{-\infty}^{+\infty}dz\, f(\zeta) = N_e$. Note that with the initial density field used here, the charge conservation equation is automatically satisfied. This model for the background fluid density is valid as long as its spatial and temporal gradients are small compared to k_0 and ω_0. The radiated photon number density now takes the form

$$\begin{aligned}\frac{d^2N_x(\omega,\hat{\mathbf{n}})}{d\omega\, d\Omega} &= \frac{\alpha}{4\pi^2}\frac{\omega}{\gamma_0^2}\rho^2\left|\int_{\mathbb{R}^2}dz\, dt\, f(\zeta)\hat{\mathbf{n}}\right.\\ &\quad\left.\times[\hat{\mathbf{n}}\times\mathbf{u}(x_\mu)]\exp[i\omega(t-\hat{\mathbf{n}}\cdot\mathbf{x})]\right|^2.\end{aligned} \tag{A24}$$

We use a Gaussian profile to obtain an analytical result for the radiated spectra; the calculations presented here can easily be generalized to other distributions. We have $f(\zeta) = \exp[-(\zeta/\Delta z)^2]$, and $\rho=N_e/\sqrt{\pi}\Delta z$, where Δz is the axial scale of the electron bunch;

$$\frac{d^2N_x(\omega_z-\hat{z})}{d\omega\, d\Omega}=\frac{\alpha}{4\pi^2}\frac{\omega}{\gamma_0^2}\rho^2A_0^2 \times\left|\int_{\mathbb{R}^2}dz\,dt\,f(\zeta)g(\phi) \times\exp\{i[\omega(t+z)-\phi]\}\right|^2. \quad \text{(A25)}$$

Here, a linearly polarized laser pulse, with temporal envelope $g(\phi)$, is considered.

The integrals over axial position and time can be separated by using $\zeta(z,t)=z-\beta_0 t$, and $\phi(z,t)=t-z$, as independent variables. The product of the differential elements is obtained using the Jacobian of the transform:

$$dz\,dt=\begin{vmatrix}\frac{\partial z}{\partial\phi} & \frac{\partial z}{\partial\zeta}\\ \frac{\partial t}{\partial\phi} & \frac{\partial t}{\partial\zeta}\end{vmatrix}d\phi\,d\zeta=-\frac{d\phi\,d\zeta}{1-\beta_0}. \quad \text{(A26)}$$

Equation (A25) now takes the simple form

$$\frac{d^2N_x(\omega_i-\hat{z})}{d\omega\, d\Omega}=\alpha\chi\rho^2A_0^2\left|\int_{-\infty}^{+\infty}d\zeta \times\exp\left[i\frac{2\chi\zeta}{1+\beta_0}-\frac{\zeta^2}{\Delta z^2}\right]\int_{-\infty}^{+\infty}d\phi \times\exp\left[i(\chi-1)\phi-\frac{\phi^2}{\Delta\phi^2}\right]\right|^2. \quad \text{(A27)}$$

The first integral can be identified as the fluid coherence factor, while the second integral corresponds to the spectral density of the Doppler-shifted Compton backscattered line. Performing the integrals over ϕ and ζ [53], we finally obtain

$$\frac{d^2N_x(\omega,-\hat{z})}{d\omega\, d\Omega}=\frac{\alpha}{16\pi}\chi A_0^2\Delta\phi^2N_0^2\exp\left[-2\left(\frac{\chi\Delta z}{1+\beta_0}\right)^2\right] \times\exp\left[-\frac{(\chi-1)^2\Delta\phi^2}{2}\right]. \quad \text{(A28)}$$

The physics of this solution can be understood as follows: the photon number density radiated on-axis scales linearly with the laser pulse energy $A_0^2\Delta\phi$, and quadratically with the number of electrons in the bunch, while the coherence factor scales exponentially with the inverse electron bunch duration squared, measured in units of the Doppler upshifted wavelength. This indicates that long electron bunches radiate incoherently at short wavelengths; also note that the fluid incoherent radiation scaling is quite different from the simple N_e scaling: it is a function of frequency, and shows very strong (i.e., exponential) suppression of short wavelengths. Finally, the Compton backscattered spectral linewidth is determined by the laser pulse linewidth $\sqrt{2}/\Delta\phi$, and its frequency is obtained for $\chi=1$. This corresponds to the frequency $\omega=[\gamma_0(1-\beta_0)]^2$; for $\beta_0\to-1$, we recover the result $\omega=4\gamma_0^2$ [21,52].

The stochastic electron gas and relativistic fluid models are compared by inspecting Eqs. (A14) and (A28), in a frame where the initial electron distribution is at rest ($\beta_0=0$). The difference between these theoretical models is shown in Fig. 13 (bottom), where the number of electrons has been chosen as $N_e=10^{10}$. The logarithm of both coherence factors is calculated as a function of the normalized electron distribution axial scale length, $\omega\Delta z$. In the case of a perfectly coherent radiation process, where $\omega\Delta z\to 0$, both models yield the well-known N_e^2 scaling. When the electron distribution becomes long compared to the radiation wavelength, the stochastic electron gas model correctly predicts the linear scaling with N_e. The fluid model yields a very different result: the coherence factor continues to decrease exponentially, as shown by the parabolic curve in Fig. 13 (bottom). This is due to the fact that the Fourier transform of the Gaussian fluid distribution is a Gaussian with an argument proportional to the product $\omega\Delta z$: for arbitrarily short wavelengths, the fluid 4-current yields a vanishingly small Fourier component. The fluid model introduces an unphysical cutoff scale given by the length of the electron distribution. Thus, the fundamental difference between the stochastic electron gas approach and the relativistic fluid model resides in the fact that, for any number of incoherently phased point electrons, the 4-current contains Fourier components at arbitrarily short wavelengths, whereas the fluid model introduces an unphysical cutoff scale. Therefore, the discrete nature of electric charge is shown to play a fundamental role in the physics of incoherent radiation processes.

3. Harmonics

In Compton scattering, harmonic production is directly related to a modulation of the Doppler-shift term in the radiation equation: as discussed earlier, the spectral brightness for a single electron is given by

$$\frac{d^2N_x(\omega,\hat{\mathbf{n}})}{d\omega\, d\Omega}=\frac{\alpha}{4\pi^2}\frac{\omega}{\kappa_0^2}\left|\int_{-\infty}^{+\infty}\hat{\mathbf{n}}\times[\hat{\mathbf{n}}\times\mathbf{u}(\phi)] \times\exp\{i\omega[\phi+z(\phi)-\hat{\mathbf{n}}\cdot\mathbf{x}(\phi)]\}d\phi\right|^2; \quad \text{(A29)}$$

therefore, the position of the radiating electron is required to determine the spectral brightness of the scattered light, as shown in the Doppler shift term, corresponding to the argument of the exponential in Eq. (A29); this is obtained by performing the following integral: $x_\mu(\phi)=x_{\mu 0}+\kappa_0^{-1}\int_0^\phi u_\mu(\vartheta)d\vartheta$. At this point, a number of important remarks are in order: first, for a number of radiating electrons, the various initial positions must be taken into account; this forms the basis of the stochastic electron gas (SEG) theory of coherence in Compton scattering presented in Sec. 1 of this appendix. Second, the linear motion of the electron in the laser field yields a modulation of the Doppler shift, which is

at the origin of harmonics radiated off-axis, as discussed in detail by Ride, Esarey, and Baine in Ref. [18]. Finally, at higher intensities, in the so-called relativistic intensity regime, the ponderomotive force modulates the axial motion of the electron; this results in the radiation of harmonics on-axis, as extensively discussed by Hartemann and Kerman [20,21], this nontrivial effect has recently been measured experimentally by Umstadter and his group [65].

In the case of circular polarization, the dimensionless vector potential takes the form $\mathbf{A}_\perp(\phi)=A_0 g(\phi)[\hat{x}\sin\phi+\hat{y}\cos\phi]$, which implies that the magnitude of the 4-vector potential varies adiabatically as the pulse intensity envelope: $A_\mu A^\mu=\mathbf{A}_\perp^2(\phi)=A_0^2 g^2(\phi)$. Furthermore, for a hyperbolic secant pulse, the full nonlinear spectrum can also be determined analytically [53] with $g(\phi)=\cosh^{-1}(\phi/\Delta\phi)$, the electron's axial position is

$$\int_{-\infty}^{\phi}\mathbf{A}_\perp^2(\psi)d\psi=\int_{-\infty}^{\phi}\frac{A_0^2}{\cosh^2\left(\frac{\psi}{\Delta\phi}\right)}d\psi$$
$$=A_0^2\Delta\phi\left[1+\tanh\left(\frac{\phi}{\Delta\phi}\right)\right]. \qquad \text{(A30)}$$

and the nonlinear backscattered spectrum is now proportional to

$$\chi\left|A_0 e^{i_z A_0^2\Delta\phi}\int_{-\infty}^{+\infty}\frac{\hat{x}\cos\phi+\hat{y}\sin\phi}{\cosh\left(\frac{\phi}{\Delta\phi}\right)}\times\exp\left\{i\chi\Delta\phi\left[\frac{\phi}{\Delta\phi}+A_0^2\tanh\left(\frac{\phi}{\Delta\phi}\right)\right]\right\}d\phi\right|^2. \qquad \text{(A31)}$$

The Fourier transform can be evaluated analytically by performing two changes of variables, namely, we first set $y=e^{\phi/\Delta\phi}$, then $x=(y^2-1)/(y^2+1)$, with the result that

$$\frac{d^2N_x(\omega,-\hat{z})}{d\omega\, d\Omega}=\frac{\alpha}{8}\chi A_0^z\Delta\phi^2\left\{\sum_{\pm}\left|\frac{\Phi(\mu_\pm,1,2iA_0^2\chi\Delta\phi)}{\cosh\left[\frac{\pi}{2}\Delta\phi(\chi\pm1)\right]}\right|^2\right\}. \qquad \text{(A32)}$$

Here Φ is the degenerate (confluent) hypergeometric function [53,66], and $\mu_\pm=\frac{1}{2}[1+i\Delta\phi(\chi\pm1)]$. The downshift of the Compton backscattered line due to radiation pressure is determined by considering the nonlinear phase in the Fourier integral: the argument of the complex exponential takes the form $\Lambda(\phi)=(\chi-1)\phi+\chi A_0^2\Delta\phi\tanh(\phi/\Delta\phi)$; we Taylor expand this nonlinear phase around $\phi=0$ by using the fact that $\tanh x\simeq x$, to obtain $\Lambda(\phi)\simeq[\chi(1+A_0^2)-1]\phi+O(\phi^3)$. The frequency of the main Compton backscattered line is obtained by canceling the linear coefficient of the expansion, which yields $\chi=(1+A_0^2)^{-1}$; this can be recast in the more familiar form

$$\omega=\frac{1}{1+A_0^2}\left(\frac{1-\beta_0}{1+\beta_0}\right)\simeq\frac{4\gamma_0^2}{1+A_0^2},$$

where the last equality holds for $\beta_0\to-1$. This is the well-known radiation frequency for an FEL with an electromagnetic wiggler [21,52].

Finally, we note that temporal shaping of the drive laser pulse can increase the contrast between the main radiated line and the satellites produced by the transient during the rise and fall of the pulse: we have demonstrated theoretically that square optical pulses, such as those studied experimentally by Weiner *et al.* [67], could be used to efficiently filter the spectral content radiated on-axis, in the case of a circularly polarized laser pulse.

4. Radiative corrections

Radiative corrections correspond to the electron interaction with the electromagnetic fields it scatters, and can be treated using quantum electrodynamics (QED), or classically, using the Dirac-Lorentz equation [20,39,50]. The latter equation describes the covariant dynamics of a classical point electron, including the radiation reaction effects due to the electron self-interaction. The main steps of Dirac's derivation are briefly outlined here; for conciseness, we now use the classical electron radius r_0 to measure length, and the corresponding time unit r_0/c. In these units, the vacuum permittivity is $\varepsilon_0=1/4\pi$, and its permeability is $\mu_0=4\pi$. The electron 4-current density is

$$j_\mu^s(x_\lambda)=-\int_{-\infty}^{+\infty}u_\mu(x'_\lambda)\delta_4(x_\lambda-x'_\lambda)d\tau', \qquad \text{(A33)}$$

and the corresponding self-electromagnetic field $F_{\mu\nu}^s=\partial_\mu A_\nu^s-\partial_\nu A_\mu^s$ satisfies the driven wave equation, $\Box A_\mu^\lambda(x_\lambda)=-4\pi j_\mu^s(x_\lambda)$, which can be solved in terms of Green's function; as

$$A_\mu^s(x_\lambda)=4\pi\int_{-\infty}^{+\infty}u_\mu(x'_\lambda)G(x_\lambda-x'_\lambda)d\tau'.$$

The self-force on the electron can now be evaluated as

$$F_\mu^s=-(\partial_\mu A_\nu^s-\partial_\nu A_\mu^s)u^\nu$$
$$=-\int_{-\infty}^{+\infty}u^\nu(x_\lambda)[u_\nu(x'_\lambda)\partial_\mu-u_\mu(x'_\lambda)\partial_\nu]G(x_\nu-x'_\nu)d\tau'. \qquad \text{(A34)}$$

The advanced and retarded Green's functions both depend on the space-time interval

$$s^2=(x-x')_\mu(x-x')^\mu:$$

$$G^\pm=-\delta(s^2)\left[1\mp\left(\frac{x_0-x'_0}{|x_0-x'_0|}\right)\right].$$

As a result, the partial derivatives can now be replaced by the operator $\partial_\mu=2(x_\mu-x'_\mu)(\partial/\partial s^2)$, and Eq. (A34) reads

$$F^s_\mu = -2\int_{-\infty}^{+\infty} u^\nu(x_\lambda)[u_\nu(x'_\lambda)(x_\mu - x'_\mu) - u_\mu(x'_\lambda)(x_\nu - \chi'_\nu)]\frac{\partial G}{\partial s^2}d\tau'. \tag{A35}$$

At this point, the new variable $\tau'' = \tau - \tau'$ is introduced, so that the range of integration explicitly includes the electron (singular point $\tau''=0$). To evaluate the integral in Eq. (A35), one can now use Taylor-McLaurin expansions in powers of τ'':

$$x_\mu - x'_\mu = \tau'' u_\mu - \tfrac{1}{2}\tau''^2 a_\mu + \tfrac{1}{8}\tau''^3 d_\tau a_\mu + \cdots$$
$$u_\mu(x'_\lambda) = u_\mu(\tau - \tau'') = u_\mu - \tau'' a_\mu + \tfrac{1}{2}\tau''^2 d_\tau a_\mu + \cdots \tag{A36}$$

where the 4-acceleration $a_\mu = d_\tau u_\mu$. Using the above expansions, one first finds that $s^2 = -\tau''^2$, which yields $\partial G/\partial s^2 \simeq -(1/2\tau'')(\partial G/\partial \tau'')$. With this, the expression for the self-electromagnetic force now reads

$$F^s_\mu = \int_{-\infty}^{+\infty}\left\{-\frac{\tau''}{2}a_\mu + \frac{\tau''^2}{3}\left[\frac{da_\mu}{d\tau} - u_\mu(a_\nu a^\nu)\right]\right\}\frac{\partial G}{\partial \tau''}d\tau''. \tag{A37}$$

This equation can be integrated by parts; using the retarded (causal) Green's function, one finds

$$F^s_\mu = -\frac{1}{2}a_\mu\int_{-\infty}^{+\infty}\frac{\delta(\tau'')}{|\tau''|}d\tau'' + \frac{2}{3}\left[\frac{da_\mu}{d\tau} - u_\mu(a_\nu a^\nu)\right]. \tag{A38}$$

The corresponding 4-momentum transfer equation now reads

$$\left[1 + \frac{1}{2}\int_{-\infty}^{+\infty}\frac{\delta(\tau'')}{|\tau'|}d\tau''\right]a_\mu = -F_{\mu\nu}u^\nu + \tau_0\left[\frac{da_\mu}{d\tau} - u_\mu(a_\nu a^\nu)\right], \tag{A39}$$

where $\tau_0 = \frac{2}{3}$ is the Compton time scale, in the units of r_0/c used here. The divergent integral on the left-hand side of the equation is the infinite electromagnetic mass of the point electron, which multiplies the 4-acceleration. Dirac first proposed [39] to renormalize this term away by using the time symmetrical Green function $G = \frac{1}{2}(G^+ - G^-)$; with this one obtains the Dirac-Lorentz equation:

$$a_\mu = -F_{\mu\nu}u^\nu + \tau_0\left[\frac{da_\mu}{d\tau} - u_\mu(a_\nu a^\nu)\right]. \tag{A40}$$

One of the conceptual difficulties associated with this equation is the existence of unphysical, runaway solutions: contracting Eq. (A40) with a^μ, it is easily seen that in the absence of an external field it reduces to

$$a_\mu a^\mu = \frac{\tau_0}{2}\frac{d}{d\tau}(a_\mu a^\mu),$$

which admits the runaway solution

$$[a_\mu a^\mu](\tau) = [a_\mu a^\mu]_0 \exp\left(2\frac{\tau}{\tau_0}\right).$$

To avoid these unphysical solutions, one must require that the Dirac-Rohrlich (DR) asymptotic condition [39,68] be satisfied: $\lim_{\tau\to\pm\infty} a_\mu(\tau) = 0$.

Also note that the second radiative correction term corresponds to the radiated 4-momentum H_μ; thus we can rewrite Eq. (A40) as

$$a_\mu = -F_{\mu\nu}u^\nu + \tau_0\frac{da_\mu}{d\tau} - \frac{dH_\mu}{d\tau}. \tag{A41}$$

In the case of an external electric field deriving from a static potential, the timelike component of the Dirac-Lorentz equation, which describes energy conservation, takes the simple form

$$\frac{d\gamma}{d\tau} = \mathbf{u}\cdot\nabla\varphi + \tau_0\frac{d^2\gamma}{d\tau^2} - \frac{dH_0}{d\tau} = \frac{d}{d\tau}\left[\varphi + \tau_0\frac{d\gamma}{d\tau} - H_0\right], \tag{A42}$$

and can be formally integrated to yield the conservation law

$$\Delta(\gamma - \varphi + H_0) = \tau_0\left[\frac{d\gamma}{d\tau}\right]_{-\infty}^{+\infty}, \tag{A43}$$

which indicates that, provided the DR asymptotic condition $\lim_{\tau\to\pm\infty}[d\gamma/d\tau] = 0$ is satisfied, the electron potential energy is converted into kinetic energy and radiation.

In the case of nonlinear Compton scattering, the Dirac-Lorentz equation can be given as

$$a_\mu = L_\mu + \tau_0\left[\frac{da_\mu}{d\tau} - u_\mu(a_\nu a^\nu)\right],$$
$$\mathbf{L}_\perp = \kappa\mathbf{E}_\perp, \quad L_z = L_0 = \mathbf{u}_\perp\cdot\mathbf{E}_\perp, \tag{A44}$$

where we recognize the light-cone variable $\kappa = \gamma - u_z$, and the laser transverse electric field. $\tau_0 = \frac{2}{3}r_0/c = 0.626 \times 10^{-23}$ s is the Compton time scale. Subtracting the axial component of Eq. (A44) from the temporal component, we obtain an equation governing the evolution of κ,

$$\frac{d\kappa}{d\tau} = \tau_0\left[\frac{d^2\kappa}{d\tau^2} - \kappa(a_\nu a^\nu)\right]. \tag{A45}$$

Introducing the small parameter $\varepsilon = \omega_0\tau_0$, which measures the Doppler-shifted laser wavelength in units of r_0, and noting that $\mathbf{E}_\perp = \varepsilon d\mathbf{A}_\perp/d\phi$, we also obtain an equation governing the evolution of the canonical momentum:

$$\frac{d}{d\tau}(\mathbf{u}_\perp - \mathbf{A}_\perp) = \tau_0\left[\frac{d^2\mathbf{u}_\perp}{d\tau^2} - \mathbf{u}_\perp(a_\nu a^\nu)\right]. \tag{A46}$$

Now using the laser phase ϕ as the independent variable, Eq. (A45) reads

$$\frac{d\kappa}{d\phi}=\varepsilon\left[\frac{d^2}{d\phi^2}\left(\frac{\kappa^2}{2}\right)-\kappa^2\left(\frac{du_\mu}{d\phi}\frac{du^\mu}{d\phi}\right)\right]. \tag{A47}$$

Since the right-hand side of Eq. (A47) is at least of order ε, we can replace the terms in the brackets with their zeroth-order (Lorentz dynamics) approximation; in this case, we obtain a simple differential equation for the light-cone variable perturbation

$$\frac{d}{d\phi}\left[\frac{1}{\kappa(\phi)}\right]\simeq\varepsilon A_0^2 g^2(\phi), \tag{A48}$$

where we recognize the envelope of the circularly polarized laser pulse. Equation (A48) can easily be integrated to yield

$$\frac{1}{\kappa(\phi)}=\frac{1}{\kappa_0}+\varepsilon A_0^2\int_{-\infty}^{\phi} g^2(\psi)d\psi. \tag{A49}$$

This last equation describes the electron recoil from the coherent laser field; it is clear that at sufficient intensities and short wavelengths, the relative radiative energy loss becomes significant.

Finally, the Dirac-Lorentz equation can be integrated backward in time to avoid runaways due to the electromagnetic mass renormalization [21,68], and the Compton backscattered spectrum is obtained by evaluating

$$\frac{d^2N_x(\varpi,-\hat{z})}{d\varpi\, d\Omega}=\frac{\alpha}{4\pi^2}\varpi\left|\int_{-\infty}^{+\infty}\frac{\mathbf{u}_\perp(\phi)}{\kappa(\phi)}\times\exp\left\{i\varpi\left[\phi+2\int_{-\infty}^{\phi}\frac{u_z(\psi)}{\kappa(\psi)}d\psi\right]\right\}\right|^2. \tag{A50}$$

5. X-ray protein crystallography

As discussed in Sec. VI, one important application identified and targeted for the 0.9-Å Compton x-ray source is protein crystallography. Proteins are highly structured and complex polymers of L-amino (left-handed) acids, linked together by peptide bonds. Three-dimensional, structured proteins are produced from their linear DNA templates in a complex transcription and subsequent ribosomal translation process.

The importance of structural knowledge cannot be overemphasized as the molecular structure of proteins determines an extremely wide variety of functions: enzymes catalyze biochemical reactions; membrane receptor proteins signal to the cell interior when a ligand binds; transport and storage proteins, such as hemoglobin and ferritin, distribute metal ions or chemicals throughout the body; structural proteins, including collagen and keratin, and muscle fibers, such as actin and myosin, play an important role in the architecture of multicellular organisms; nutritional proteins provide amino acids for growth (e.g., casein and ovalbumin); antibody proteins are essential components of the immune system; finally, regulatory proteins such as transcription factors, bind to and modulate the transcription of DNA. Human DNA contains approximately 3×10^9 base pairs, which code for over 100 000 different proteins.

A. Multiwavelength anomalous diffraction

The basic elements behind MAD phasing are presented in Sec. VI A; here we note that before the introduction of MAD, the isomorphous replacement method was successfully used to obtain the structure of complex proteins; for example, urease was studied by Jabri *et al.* [57], with 40 heavy atom compounds screened to find five sufficiently isomorphous derivatives of the crystal: $HOHgC_6H_4CO_2Na$, $EuCl_2$, $Hg_2(CH_3COO)_2$, $C(HgOOCCH_3)_4$, and $(CH_3)_3Pb(CH_3COO)$ [57]. This example indicates the level of complexity and uncertainty involved in the search for multiple isomorphous heavy metal derivatives, and why MAD has quickly become the preferred method for phase determination for complex macromolecular crystals, as explained in Sec. VI.

b. HIV protease inhibitors: A case study for structure-based drug design

The recent development of powerful antiviral drugs to fight HIV has demonstrated the efficiency of x-ray protein crystallography as a powerful tool to help design new drugs *ab initio*, in sharp contrast with the previous trial-and-error approach. For example, the first generation of anti-HIV drugs includes such molecules as AZT (azidothymidine), a molecule analogous to the nucleoside thymidine; the reverse transcriptase enzyme of the virus is thus misled into using AZT instead of thymidine, which is normally paired with adenosine on the RNA chain to be transcribed. However, because of its relatively poor specificity, AZT also inhibits the cellular polymerase of mitochondria, which produce adenosine triphosphate (ATP); this explains the serious side effects of this drug, including severe muscle fatigue and anemia [36]. Similarly, other reverse transcriptase inhibitors have been synthesized and administered to AIDS patients, including ddl (a precursor to ddA, an analog to deoxyadenosine), and ddC (an analog to deoxycytosine); both are toxic, causing neurological problems, including polyneuritis. More recently, equally active and somewhat less toxic drugs have been introduced, such as 3TC, an analog of cytosine, d4T, an analog of thymidine, and non-nucleoside analogs, such as TIBO inhibitors [36]. Combining such drugs, at lower doses, helps minimize the aforementioned side effects; however, the most dramatic improvements have been obtained after the HIV protease structure has been determined by x-ray crystallography: with the knowledge of atomic details within the catalytic site of the HIV protease, a novel family of small molecular drugs, called protease inhibitors, has been designed and synthesized *ab initio*, with high specificity to the aspartyl binding sites of the HIV protease. These new drugs have been very successful, especially when used in conjunction with the aforementioned reverse transcriptase and integrase inhibitors (the so-called ''triple therapy''), in reducing the viral load in some patients below the detection threshold of enzyme-linked immunosorbent assays [37].

c. Protein data acquisition time

In Sec. VI B, basic considerations were taken into account to give a first comparison of the average x-ray brightness produced by different sources. In this section, we first briefly recapitulate the aforementioned results; we then elaborate and refine this discussion in much greater detail.

In terms of the spectral brightness requirement for the data acquisition time, a few preliminary comments are in order. First, the current average cost for the determination of the three-dimensional structure of a protein is approximately \$200,000 [31]; given the number of proteins coded for by human DNA, which is estimated to be on the order of 10^5, new technologies are clearly required to complete a genome-wide structural analysis of proteins (structural genomics) [31]. We also note that the average cost of a synchrotron beamline is \$8,000,000; smaller, less expensive sources could be extremely useful in terms of added flexibility, even at lower average spectral brightness. Second, the amount of time currently required to isolate and amplify the target sequence, crystallize the corresponding protein, acquire the x-ray diffraction data at different wavelengths for MAD phasing, post-process the data, and build a structural model into the electron density map, range between 1 and 6 months; therefore, an acquisition time of a few tens of hours is quite acceptable; in fact, a reasonable target would be to determine 50–100 structures/year on a compact device. Finally, extremely high flux, such as that produced by insertion devices on third-generation synchrotrons, frequently causes radiation damage in the biological material and loss of the crystal even in properly cryocooled specimens. Consequently, strong attenuation of the beam becomes necessary [59].

A first, simple comparison can be made by considering the average spectral brightness of different sources; the results are typically given in units of photons/0.1% bandwidth/mm^2/mrad^2/s [29]. For modern rotating anode sources, given a 2.6-eV width for the $K_{\alpha 1}$ line of copper at 1.540 51 Å, and up to 98% flux in that line, an average brightness around 10^9 is possible; synchrotron bending magnets reach 10^{15} at 10 keV for a 6–8-GeV ring, while a 72-period, 3.3-cm wavelength undulator produces 9.4-keV photons with a brightness of 4.8×10^{18} at the APS [29]; however, brightnesses $>10^{12}$ begin to cause severe radiation damage. The Compton source generates 12.77-keV photons with a brightness of 4.1×10^{10}; this compares quite favorably with rotating anode x-ray sources, especially in view of added tunability, which is indispensable for MAD.

A more detailed comparison between the Compton source and conventional rotating anode x-ray sources will now be given, where the protein diffraction acquisition time is evaluated in each case. We start from a known, state-of-the-art, rotating anode x-ray source with Osmic MaxFlux® confocal multilayer fixed-focus optical system [60]: the flux through a 0.5-mm-diameter collimator is measured at 2.5×10^9 photons/(mm^2 s) [61]. The corresponding flux on the sample is 5×10^9 photons/s, and the total data acquisition time is 2.16×10^4 s, in high-resolution mode; including absorption and other losses, the total number of photons diffracted by the sample is 1.08×10^{13}. Depending on the resolution (the diffraction limit in the 2θ angle, expressed as the smallest observed d-spacing), 10^4-10^5 unique reflections are routinely collected for molecules weighing a few tens to a few hundred kiloDa (for example, lysozyme, space group $P4_3\,2_1\,2$, molecular weight of 14.5 kDa, 19 500 unique reflections to a typically good resolution of 1.5 Å, 39 000 reflections for both Friedel wedges). The collection of these reflections requires a systematic, careful scanning of a large solid angle, with a sufficient integration time at each step to bring the signal-to-noise ratio to a desired value [usually $I/\sigma(I)=2$ in the highest resolution shell; in our example 1.5 Å], which determines the data acquisition time. Using a typical number of 1.95×10^4 unique reflections for lysozyme, we see that the highest-resolution mode requires approximately 5.5×10^5 photons/reflection ($\sigma=20.1$, which is excellent); furthermore, the signal-to-noise ratio scales as the square root of this number. The Compton source produces an average flux of 2.5×10^7 photons/s in a 1-eV spectral interval, quite sufficient for MAD, that can be captured in a 3.5-mrad angle, which is much smaller than the 1° (17 mrad) acceptance angle of the aforementioned confocal mirrors [61]. For 10^8 photons/reflection ($\sigma=18.4$), the acquisition time is estimated at 10 h/10^4 reflections. These results are in line with a goal of 50–100 structures a year: a full 3-wavelengths MAD scan could be completed in 60 h. We also note that our results are preliminary, and that we are in the process of designing an optimized source for this application.

d. The micro-MAD concept

A unique characteristic of the Compton source is the very small size of the x-ray source, which essentially matches that of the laser focal spot size; for imaging applications, this translates into increased contrast and better resolution. This also has important implications for microcrystals, which are more easily produced and often are of better quality (i.e., diffracting to higher resolution with smaller mosaicity) than larger ones. Cooling also becomes less problematic in smaller crystals due to the lower amount of heat generated and the more advantageous surface-to-volume ratios. Therefore, the Compton x-ray source seems almost ideally suited for the development of a compact, user-friendly, tunable x-ray source, with an average brightness comparing well with that of rotating anode sources, and the capability of using MAD on microcrystals; this is the idea underlying the micro-MAD (μMAD) concept currently being evaluated at Lawrence Livermore National Laboratory.

e. Practical issues

One important issue related to the concept discussed above are the background x-rays produced by the electron beam line and dump. The beam halo produces bremsstrahlung x-rays over a broad energy range, which contribute to the background noise on the detectors; this problem can be partially alleviated by using a magnetic chicane before the

Compton interaction region. In terms of shielding, the electron source is similar to a clinical linac, although the average current is somewhat lower; therefore, we believe that it is not an insurmountable problem. In particular, it may be possible to decelerate the electron bunch in a linac section, after interaction, before the dump; this could minimize the x-ray and activation problems, and produce rf power that could potentially be recycled.

[1] M. D. Perry and G. Mourou, Science **264**, 917 (1994).
[2] G. A. Mourou, C. P. J. Barty, and M. D. Perry, Phys. Today **51** (1), 22 (1998).
[3] C. P. J. Barty *et al.*, Opt. Lett. **21**, 668 (1996).
[4] D. P. Umstadter, C. Barty, M. Perry, and G. A. Mourou, Opt. Photonics News **9**, 41 (1998).
[5] *Advanced Accelerator Concepts, 8th Workshop*, edited by W. Lawson, C. Bellamy, and D. F. Brosius, AIP Conf. Proc. No. 472 (AIP, Woodbury, NY, 1999).
[6] D. Yu *et al.*, *Advanced Accelerator Concepts* (Ref. [5]).
[7] S. G. Biedron *et al.*, *Advanced Accelerator Concepts* (Ref. [5]).
[8] R. W. Schoenlein *et al.*, Science **274**, 236 (1996).
[9] W. P. Leemans *et al.*, Phys. Rev. Lett. **77**, 4182 (1996).
[10] W. P. Leemans *et al.*, IEEE J. Quantum Electron. **QE11**, 1925 (1997).
[11] C. Bula *et al.*, Phys. Rev. Lett. **76**, 3116 (1996).
[12] D. Burke *et al.*, Phys. Rev. Lett. **79**, 1626 (1997).
[13] C. Bamber *et al.*, Phys. Rev. D **60**, 092004 (1999).
[14] V. N. Litvinenko *et al.*, Phys. Rev. Lett. **78**, 4569 (1997).
[15] W. Greiner and J. Reinhardt, *Quantum Electrodynamics* (Springer-Verlag, Berlin, 1994), Chap. 3.7.
[16] E. Esarey, S. K. Ride, and P. Sprangle, Phys. Rev. E **48**, 3003 (1993).
[17] F. V. Hartemann *et al.*, Phys. Rev. E **54**, 2956 (1996).
[18] S. K. Ride, E. Esarey, and M. Baine, Phys. Rev. E **52**, 5425 (1995).
[19] E. Esarey, P. Sprangle, and J. Krall, Phys. Rev. E **52**, 5443 (1995).
[20] F. V. Hartemann and A. K. Kerman, Phys. Rev. Lett. **76**, 624 (1996).
[21] F. V. Hartemann, Phys. Plasmas **5**, 2037 (1998).
[22] C. W. Siders *et al.*, Science **286**, 1340 (1999); C. Rose-Petruck *et al.*, Nature (London) **398**, 310 (1999).
[23] A. H. Chin *et al.*, Phys. Rev. Lett. **83**, 336 (1999).
[24] A. M. Lindenberg *et al.*, Phys. Rev. Lett. **84**, 111 (2000).
[25] R. A. Robb, *Three-Dimensional Biomedical Imaging: Principles and Practice* (Wiley-VCH, New York, 1995).
[26] R. Fitzgerald, Phys. Today **53** (7), 23 (2000).
[27] J. Drenth, *Principles of Protein X-Ray Crystallography*, 2nd ed. (Springer-Verlag, New York, 1999).
[28] K. E. van Holde, W. Curtis Johnson, and P. Shing Ho, *Principles of Physical Biochemistry* (Prentice-Hall, Upper Saddle River, NJ, 1988), Chap. 6.
[29] D. Atwood, *Soft X-Rays and Extreme Ultraviolet Radiation* (Cambridge University Press, Cambridge, England, 1999).
[30] F. Golden and M. D. Lemonick, Time **156** (1), 19 (2000).
[31] K. Garber, Technol. Rev. **103**, 46 (2000).
[32] M. D. Lemonick, Time **156** (1), 24 (2000).
[33] B. D. Hames, N. M. Hooper, and J. D. Houghton, *Biochemistry* (Springer, New York, 1997), Sec. I.
[34] M. Balter, Science **274**, 1988 (1996).
[35] *Nucleic Acids in Chemistry and Biology*, 2nd ed., edited by G. M. Blackburn and M. J. Gait (Oxford University Press, New York, 1996).
[36] L. Montagnier, *Virus* (Norton, New York, 2000).
[37] J. Nicklin, K. Graeme-Cook, T. Paget, and R. Killington, *Microbiology* (Springer, New York, 1999), Sec. K; P. C. Turner, A. G. McLenna, A. D. Bates, and M. R. H. White, *Molecular Biology* (Springer, New York, 1998), Secs. R and S.
[38] W. A. Hendrickson and C. M. Ogata, Methods Enzymol. **276**, 494 (1997).
[39] P. A. M. Dirac, Proc. R. Soc. London, Ser. A **167**, 148 (1938).
[40] F. V. Hartemann *et al.*, Phys. Rev. E **58**, 5001 (1998).
[41] B. Quesnel and P. Mora, Phys. Rev. E **58**, 3719 (1998).
[42] F. V. Hartemann, Phys. Rev. E **61**, 972 (2000).
[43] M. J. Hogan *et al.*, Phys. Rev. Lett. **81**, 4867 (1998).
[44] M. Reiser, *Theory and Design of Charged Particle Beams* (Wiley, New York, 1994), Chaps. 3 and 6.
[45] H. Wiedemann, *Particle Accelerator Physics*, 2nd ed. (Springer, New York, 1999), Vol. 1, Chaps. 5 and 8.
[46] B. E. Carlsten, Nucl. Instrum. Methods Phys. Res. A **285**, 313 (1989).
[47] W. Pauli, *Theory of Relativity* (Dover, New York, 1958), Secs. 19, 27, and 28.
[48] R. P. Feynman, R. B. Leighton, and M. Sands, *The Feynman Lectures on Physics* (Addison-Wesley, Reading, MA, 1964), Vol. 2, Chap. 25.
[49] H. Goldstein, *Classical Mechanics*, 2nd ed. (Addison-Wesley, Reading, MA, 1980).
[50] A. O. Barut, *Electrodynamics and Classical Theory of Fields and Particles* (Dover, New York, 1980), Chaps. 3 and 5.
[51] J. D. Jackson, *Classical Electrodynamics*, 2nd ed. (Wiley, New York, 1975), Chap. 14.
[52] C. W. Roberson and P. Sprangle, Phys. Fluids B **1**, 3 (1989).
[53] I. S. Gradshteyn and I. M. Ryzhik, *Table of Integrals, Series, and Products*, 4th ed. (Academic, Orlando, FL, 1980), Eqs. 3.923, 3.924, and 3.323.3.
[54] A. D. Yeremian (private communication).
[55] S. Wolfram, *The Mathematica Book*, 3rd ed. (Wolfram Media, Champaign, IL, 1996).
[56] Los Alamos Accelerator Code Group, *Computer Codes for Particle Accelerators Design and Analysis: A Compendium*, 2nd ed. (LANL, Los Alamos, NM, 1990).
[57] E. Jabri *et al.*, Science **68**, 998 (1995).
[58] W. A. Hendrickson *et al.*, EMBO J. **5**, 1665 (1990).
[59] W. P. Burmeister, Acta Crystallogr., Sect. D: Biol. Crystallogr. **56**, 328 (2000).
[60] M. Hart and L. Berman, Acta Crystallogr., Sect. A: Found. Crystallogr. **54**, 850 (1998).
[61] L. C. Jiang, B. Verman, and K. D. Joensen, J. Appl. Crystallogr. **33**, 801 (2000).

[62] S. Ringhofer, R. Ulrich, B. Segelke, M. Knapp, and B. Rupp (unpublished).
[63] B. W. Segelke, M. Forstner, M. Knapp, S. Trakhanov, S. Parkin, Y. Newhouse, H. D. Bellamy, K. H. Weisgraber, and B. Rupp, Protein Sci. **9** (5), 886 (2000).
[64] A web-based introduction into protein crystallography, including MAD phasing techniques, can be found at http://www-structure.llnl.gov/Xray/101/index.html.
[65] S. Y. Chen, A. Maksimchuk, and D. Umstadter, Nature (London) **396**, 653 (1998).
[66] *Handbook of Mathematical Functions*, edited by M. Abramowitz and I. A. Stegun (Dover, New York, 1965), Chap. 13.
[67] A. M. Weiner *et al.*, J. Opt. Soc. Am. B **5**, 1563 (1988).
[68] F. Rohrlich, *Classical Charged Particles* (Addison-Wesley, Reading, MA, 1965), Chaps. 6 and 9.